

XMM–Newton and ESO observations of the two Unidentified γ -ray Sources 3EG J0616–3310 and 3EG J1249–8330*

N. La Palombara¹, R. P. Mignani², E. Hatziminaoglou³, M. Schirmer⁴, G.F. Bignami^{5,6}, P. Caraveo¹

¹ INAF – IASF Milano, Via E. Bassini 15, I–20133 Milano (I)

² Mullard Space Science Laboratory, University College London, Holmbury St Mary, Dorking, Surrey RH5 6NT (UK)

³ Instituto de Astrofísica de Canarias, Via Lactea, E–38200 La Laguna–Tenerife (E)

⁴ Isaac Newton Group of Telescopes, Edificio Mayantigo, Calle Alvarez Abreu 68, E–38700 Santa Cruz de la Palma (E)

⁵ Centre d’Étude Spatiale des Rayonnements (CESR), CNRS–UPS, 9 Avenue du colonel Roche, F-31028 Toulouse (F)

⁶ Università di Pavia, Dipartimento di Fisica Teorica e Nucleare, Via Ugo Bassi 6, I–27100 Pavia (I)

Abstract. The limited angular resolution of γ -ray telescopes prevents a direct identification of the majority of sources detected so far. This is particularly true for the low latitude, probably galactic, ones only 10 % of which has been identified. Most counterparts of the identified low-latitude γ -ray sources are *Isolated Neutron Stars* (INS), both *radio-loud* and *radio-quiet* (Geminga-like) objects, which are characterised by an extremely high value of the *X-ray-to-optical* flux ratio f_X/f_{opt} . Therefore, the systematic X-ray and optical coverage of low-latitude unidentified γ -ray sources aiming at high f_X/f_{opt} sources seems one of the most promising ways to spot INS candidate counterparts. Since low latitude sources are heavily affected by the interstellar absorption at both X-ray and optical wavelengths, we have focussed on two middle-latitude, probably galactic, *GRO/EGRET* sources: 3EG J0616–3310 and 3EG J1249–8330. These two sources, which could belong to a local galactic population, have been selected owing to their relatively good positional accuracy, spectral shape and lack of candidate extragalactic radio counterparts. Here we report on X-ray observations of the two γ -ray error boxes performed with *XMM–Newton* and on their optical follow-up carried on with the *Wide Field Imager* at the ESO/MPG 2.2m telescope. Less than half of the ~ 300 sources detected by the X-ray coverage have no optical counterparts. Among those, we have selected few interesting sources with $f_X/f_{\text{opt}} \geq 100$, which we consider promising INS candidates.

Key words. stars: neutron– γ -rays: observations – X-rays: general, surveys, catalogues

1. Introduction

The nature of the Unidentified γ -ray Objects (UGOs) is one of the main issues of the γ -ray astronomy. The third *Compton Gamma Ray Observatory (CGRO) EGRET* catalogue (Hartman et al. 1999) contains 271 high-energy γ -ray sources detected at energies above 0.1 GeV. The high-latitude ones ($|b| > 10^\circ$) are 191, and 93 of them have been identified with *blazars* i.e. featureless flat spectrum radio-loud AGN and BL Lac objects (von Montigny et al. 1995), while 5 of the 80 sources at low latitude have been identified with pulsating *Isolated Neutron Stars* (INSs), both classical radio-pulsars and radio-quiet, Geminga-like, objects (Caraveo 2002; Thompson 2004). In total, 170 *EGRET* sources, 74 of which at low latitudes, have no counterpart at lower frequencies and remained unidentified. The identification work had been hampered mainly by the poor localization (about 1° in diameter at

low-latitudes and up to 1.5° at mid-latitudes) which frustrated the search for counterparts at other wavelengths. Moreover, the limited γ -ray statistics made it impossible to perform ‘blind’ periodicity analysis aimed at unveiling undiscovered INSs.

The distribution analysis of the UGOs in the third *EGRET* catalogue (Figure 1) shows that they can be grouped in at least four different populations (Gehrels et al. 2000; Grenier 2000, 2001, 2004; Romero & et al. 2004). The presumably galactic UGOs (included those observed at $|b| > 10^\circ$) are equally distributed in 3 populations, with about 45 sources each. The GRP–I includes bright and relatively hard sources near the galactic plane ($|b| < 3^\circ$), with a concentration towards the inner spiral arms (Bhattacharya et al. 2003) at distances of a few kpc (Kanbach et al. 1996; Romero et al. 1999). Many of these sources are well correlated with tracers of star formation, which means that their age should be a few million years at most (Romero 2001; Grenier 2004). The GRP–II includes variable sources at $|b| > 3^\circ$ which are distributed in a sort of spherical halo around the Galactic Center with a radial distribution equivalent to that of globular clusters (Grenier 2001, 2004). These sources are softer and significantly more variable than GRP–I sources (Torres et al. 2001a,b; Nolan et al. 2003); they

* This work is based on observations obtained with *XMM–Newton*, an ESA science mission with instruments and contributions directly funded by ESA Member States and NASA. Optical observations have been obtained with the ESO/MPG 2.2m at La Silla (Chile) under programs 68.D–0478(A) and 68.D–0478(B).

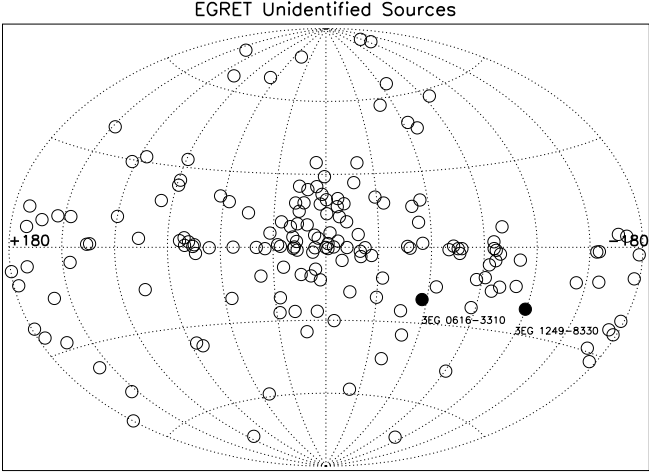


Fig. 1. Galactic distribution of the unidentified γ -ray sources from the third *EGRET* catalogue (Hartman et al. 1999): the two black circles show the positions of 3EG J0616–3310 and 3EG J1249–8330

are presumably older (with an age of the order of a few Gyrs) and at distances between 2 and 8 kpc. The last group is the *Local Gamma-Ray Population* (LGRP). It is composed by stable sources at $3^\circ < |b| < 30^\circ$, which are fainter and softer than sources located at lower Galactic latitude and have an evident asymmetric distribution north of the Galactic center and south of the anticenter. Gehrels et al. (2000) and Grenier (2000) suggested that these sources might be associated with the Gould Belt, i.e. a 30 Myr old starburst region, 300 pc in radius, composed by young massive and late type stars, molecular clouds, and expanding interstellar medium. Therefore, LGRP sources should be young (i.e. a few Myr old) nearby (100–400 pc) and low luminosity ($\sim 10^{32-33}$ erg s $^{-1}$) objects (Grenier 2004). But recently, using an improved interstellar emission model, Casandjian et al. (2005) have shown that most of these sources can correspond to the emission of clumpy dark clouds that surround all the molecular clouds of the Gould Belt; therefore their existence is not confirmed. Finally, there is an isotropic population of extragalactic origin, which is characterized by a variety of spectra and variabilities and includes no more than 35 sources.

After the release of the third *EGRET* catalogue, only a few additional identifications have been obtained. From the extragalactic point of view, the multiwavelength approach has led to a blazar identification of 3EG J2016+3657 (Halpern et al. 2001b), 3EG J2006-2321 (Wallace et al. 2002) and 3EG J2027+3429 (Sguera et al. 2004), while for 3EG 1621+8203 (Mukherjee et al. 2002), 3EG J1735-1500 (Combi et al. 2003) and 3EG J0416+3650 (Sguera et al. 2005) a radio-galaxy has been proposed as counterpart. Within the Galaxy, 3EG J1824-1514 and 3EG J0241+6103 have been associated with the two well-known microquasars LS 5039 (McSwain et al. 2004) and LS I +61 303 (Massi 2004; Casares et al. 2005), while Combi et al. (2004) suggested the association between the microquasar candidate AX J1639-4642 and the UGO 3EG

J1639-4702. In two cases a peculiar early-type binary system have been suggested as counterpart of an UGO, i.e. SAX J0635+0533 for 3EG J0634+0521 (Kaaret et al. 2000) and A0535+26 for 3EG J0542+2610 (Romero et al. 2001). Turning now to the INS family, the search for radio or X-ray pulsars has provided likely candidates for 3EG J0222+4253 (PSR J0218+4232, Kuiper et al. (2002)), 3EG J1048-5840 (PSR B1046-58, Kaspi et al. (2000)), 3EG J2021+3716 (PSR J2021+3651, Roberts et al. (2002b)) and 3EG J2227+6122 (RX/AX J2229.0+6114, Halpern et al. (2001c,a)). Moreover, thanks to the Parkes Multi-beam pulsar Survey (PMS) of the galactic plane (Manchester et al. 2001), other promising pulsar candidates have been found for 3EG J1420-6038 and 3EG J1837-0606 (D'Amico et al. 2001) and for 3EG J1013-5915 (Camilo et al. 2001). However, none of the proposed identifications could be confirmed owing to the lack of contemporary radio data. Finally, various X-ray and radio studies have pointed to a close relationship between the *pulsar wind nebulae* (PWN) and the *EGRET* sources (Roberts et al. 2002a, 2001, 2005; Roberts 2005).

Apart from the cases of Cen A and of the LMC, all the *EGRET* sources identified so far fall either in the INS or in the Blazar class. However, also in view of the *High Energy Stereoscopic System* (HESS) results which are unveiling several classes of very high energy γ -ray emitters (Aharonian et al. 2005a,b,d,c; Brogan et al. 2005), it is hard to believe that these two classes exhaust all possible γ -ray source scenarios. Nevertheless, it has been argued that rotation powered pulsars should dominate the Galactic γ -ray source population (Yadigaroglu & Romani 1997) and that many of those should be radio-quiet, since the γ -ray beam is broader than the radio one. The classic example of a radio-quiet pulsar is Geminga (Caraveo et al. 1996), which offers an elusive template behaviour: prominent in high energy γ -rays, easily detectable in X-rays but downright faint in optical, with sporadic or no radio emission (Bignami & Caraveo 1996). In the latest years, the idea that galactic UGOs might be associated with Geminga-like objects has been strengthened by the cases of three UGOs which were associated with radio-quiet INSs: 3EG J1835+5918, the brightest among the unidentified UGOs and considered ‘the next Geminga’ (Mirabal & Halpern 2001; Reimer et al. 2001; Halpern et al. 2002), and the two sources 3EG J0010+7309 and 3EG J2020+4017, positionally coincident with the supernova remnants CTA-1 (Brazier et al. 1998; Halpern et al. 2004) and γ -Cyg (Brazier et al. 1996), respectively.

The energetic of the Geminga-like objects is not sufficient to account for the very low latitude, presumably more distant, GRP-I sources but could account for several middle latitude, rather nearby, objects of the LGRP. Based on this rationale, we considered the case of two middle latitude (see Figure 1) UGOs: 3EG J0616-3310 and 3EG J1249-8330 (La Palombara et al. (2005), Paper I). Both sources are characterized by a relatively good positional accuracy, with a 95% confidence error circle radius $\theta_{95} \sim 0.6^\circ$, by a power law photon index $\Gamma \sim 2.1$ and by a steady emission with fluxes above 0.1 GeV of (12.6 ± 3.2) and $(19.9 \pm 4.4) \times 10^{-8}$ photon cm $^{-2}$ s $^{-1}$, respectively (Hartman et al. 1999). In both

Table 1. Main characteristics of the eight *EPIC* observations of 3EG J0616–3310 (ID = 1–4) and 3EG J1249–8330 (ID = 5–8)

Field ID	Rev.	Date (UT)	R.A. (J2000) <i>h m s</i>	DEC (J2000) $^{\circ}, '$ "	Exposure Time (ks)			N_{H} (10^{20} cm $^{-2}$)	Detected Sources
					PN	MOS1	MOS2		
1	346	2001-10-29T17:04:09	06 17 47.1	−32 55 13.9	6.8	11.4	11.5	2.7	50
2	341	2001-10-18T23:53:02	06 17 47.1	−33 25 13.9	6.7	12.0	12.0	2.5	37
3	346	2001-10-29T04:27:17	06 15 24.1	−33 25 13.9	2.5	7.3	7.7	2.4	32
4	346	2001-10-28T23:26:57	06 15 24.1	−32 55 13.9	1.3	6.3	7.7	2.5	27
5	236	2001-03-23T12:56:43	12 57 53.1	−83 15 01.9	7.0	11.2	11.3	10.2	38
6	236	2001-03-23T17:54:20	12 57 53.1	−83 45 01.9	8.2	11.2	10.9	8.4	51
7	239	2001-03-30T03:50:11	12 40 13.1	−83 45 01.9	0.8	2.9	2.4	9.4	7
8	239	2001-03-29T22:28:14	12 40 13.1	−83 15 01.9	8.3	12.7	12.9	11.2	52

cases, the lack of radio counterparts down to a limit of a few tens of mJy (Mattox et al. 2001; Tornikoski et al. 2002; Sowards-Emmerd et al. 2004) does not support an extragalactic identification, while an association with the Gould Belt appears more likely (their existence was confirmed also by Casandjian et al. (2005)). Thus we have applied the multi-wavelength approach successfully used for the identification of Geminga as well as for other UGOs associated with radio-quiet INS (Caraveo 2001; Mukherjee & Halpern 2004). In the multiwavelength approach, we start with the X-rays since they are the nearest neighbours to γ -rays and can be used to bridge the gap between the poor resolution achievable in γ -rays and the standards of optical or radio astronomy. First, an X-ray image of the γ -ray error-box is taken and the detected X-ray sources are cross-correlated with optical and radio catalogues, either available in archives or produced from *ad hoc* observations. Next, potential INS candidates are singled out amongst X-ray sources with an extremely high value of the *X-ray-to-optical* flux ratio $f_{\text{X}}/f_{\text{opt}}$. This ‘top-down’ systematic strategy is a time consuming exercise since it usually involves several observing cycles with different instruments at different facilities, both space and ground-based. Thus it can be pursued for a large number of γ -ray sources only if a semi-automatic procedure is set-up. Our work can be viewed as a preparatory step for the massive identification work which will be needed in the coming years, when *AGILE* (Tavani et al. 2003) and *GLAST* (McEnery et al. 2004) will deliver hundreds of new γ -ray sources. The improved angular resolution of these new γ -ray telescopes will provide arcmin positioning, thus easing considerably the identification work. To this aim, a statistical approach will be necessary (Torres & Reimer 2005).

X-ray observations and data reduction techniques are presented in §2, while the X-ray source analysis is described in §3. The optical observations are described in §4, while the cross-correlations of the X-ray data with the optical and radio ones are described in §5. In §6 we discuss the source X-ray/optical analysis, while the most interesting sources are presented in §7. Finally, in §8 summary and conclusions are outlined.

2. X-ray observations

The error boxes of 3EG J0616–3310 and 3EG J1249–8330 are circles of ~ 35 arcmin radius, a value comparable to the field of view of the *XMM-Newton* telescopes (Jansen et al. 2001).

Furthermore, with an unprecedented collecting area of ~ 2500 cm 2 @ 1 keV, a good spectral resolution ($\sim 6\%$ @ 1 keV) and a rather broad energy range (0.1–10 keV), the *European Photon Imaging Camera (EPIC)*, is particularly suited to investigate faint sources. Therefore, we covered each *EGRET* error box with four $\simeq 10$ ks *EPIC* observations (see Paper I), corresponding to $\sim 70\%$ of the 95 % error circle. They did not cover the central part of the error circle, which is not a favoured region for the true position of the γ -ray source. Therefore, the probability that it was actually covered by our observations depends only on their geometry and is $\sim 70\%$. In each observation all the three *EPIC* focal plane cameras were active: the *PN* camera (Strüder et al. 2001) was operated in Extended Full Frame mode, while the *MOS1* and *MOS2* cameras (Turner et al. 2001) were operated in standard Full Frame mode. In all cases the thin filter was used. The details of the eight observations are listed in Table 1 where, for each of them, we report the pointing coordinates, the ‘effective’ exposure times of the three cameras after the soft-proton rejection (§2.1), the galactic neutral hydrogen column density in the pointing direction, and the total number of detected sources.

2.1. Data Processing

For each pointing we obtained three data sets, one for each camera, which were independently processed through the standard *XMM-Newton Science Analysis System (SAS)* v.5.2. In the first step, the *XMM/SAS* tasks *emproc* and *epproc* were used to linearize the *MOS* and *PN* event files, respectively. In the second step, event files were cleaned up for the effects of hot pixels and soft proton flares.

Hot pixels, flickering pixels and bad columns, which produce spurious source detections during an observation, are largely removed by the on board data processing software while the remaining ones are masked by the *XMM/SAS*. However, we found that several spurious events were still present in the processed data. These have been localized using the *IRAF* task *cosmicrays* and removed using the multipurpose *XMM/SAS* task *evselect*. We then filtered out time intervals affected by high instrument background induced by soft proton flares (energies less than a few hundred keV) hitting the detector surface. To this aim, we accumulated the light curves of the events selected close to the CCDs edges and with energies greater than 10 keV to avoid contributions from real X-ray source

variability. For the *PN* data we considered only single pixels events (PATTERN = 0) with energies 10–13 keV while for the *MOS* data we considered both single and double pixels events (PATTERN ≤ 4) with energies 10–12.4 keV in CCDs 2–7. Then, we set a count rate threshold for good time intervals at 0.15 and 0.35 cts s^{-1} for the *MOS* and the *PN* data, respectively. By selecting only events within the ‘good’ time intervals we finally obtained three ‘clean’ event lists for each observation, whose ‘effective’ exposure times are reported in Table 1. As can be seen, the space weather was not favourable during the observation of field 7 (which was so much affected by the high particle background that we lost up to 80 % of the integration time) and, partly, for the observations of fields 3 and 4. An example of the processed *EPIC/MOS* image is shown in Figure 2, in the case of field 4.

2.2. Source Detection

In order to increase the *signal to noise* (S/N) ratio for the detected sources and to reach fainter X-ray fluxes, for each observation we used the *XMM/SAS* task *merge* to merge the clean linearized event lists of the 3 cameras. This was possible thanks to the excellent relative astrometry between the *MOS* and the *PN* ($\sim 1''$, a value much smaller than the FWHM of the PSF). In such a way we obtained a ‘total’ event list, which was used to generate images in 7 different energy ranges. Namely, we considered two standard coarse soft/hard bands (0.5–2 and 2–10 keV) and a finer energy division (0.3–0.5, 0.5–1, 1–2, 2–4.5, 4.5–10 keV). All images were built with a spatial binning of $4''.35$ per pixel, roughly matching the physical binning of the *PN* images ($4''/\text{pixel}$) and a factor about four larger than the one of the *MOS* images ($1''.1/\text{pixel}$). For each energy band, a corresponding set of exposure maps (i.e. one for each of the three detectors) was generated with the *XMM/SAS* task *expmap*, to account for spatial quantum efficiency (QE), mirror vignetting and field of view. Finally, the individual detector maps were merged in order to obtain the ‘total’ exposure map for the relevant energy range. Both images and exposure maps were used as a reference for the source detection, which was performed in three steps:

1. For each of the selected energy bands, the *XMM/SAS* task *eboxdetect* was run in *local mode* to create a preliminary source list. Sources were identified by applying the standard *minimum detection likelihood* criterium, i.e., only candidate sources with detection likelihood $-\ln P \geq 5$, where P is the probability of a spurious detection due to a Poissonian random fluctuation of the background, were validated.
2. Then, the task *esplinemap* was run to remove all the validated sources from the original image and to create a background map by fitting the so called *cheesed image* with a cubic spline.
3. Finally, for each of the selected energy bands the task *eboxdetect* was run again, but in *map mode* using as a reference the calculated background maps. The likelihood values from each individual energy band were then added and transformed to *equivalent single band* detection likelihoods, with a threshold value of 10 applied to accept or reject a detected source.

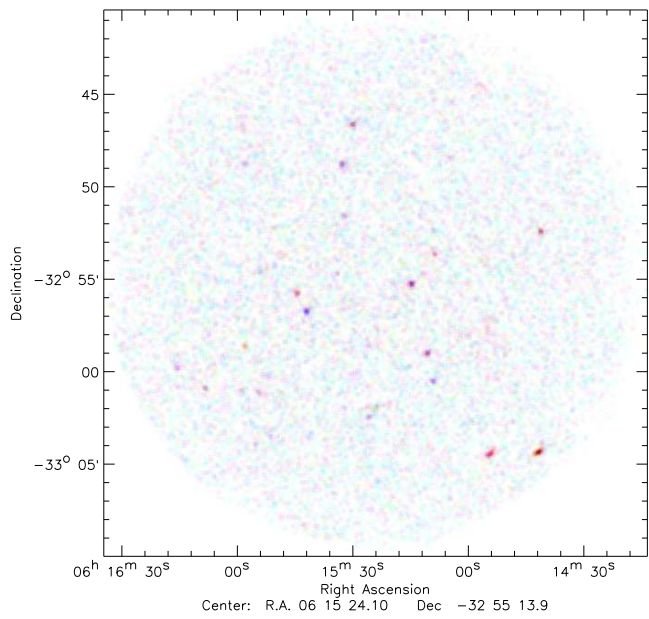


Fig. 2. Processed XMM-Newton *EPIC/MOS* image of field 4 (see Table 1). Photons selected from three different energy bands are colour-coded: red (0.3–1 Kev); green (1–3 Kev); blue (3–10 Kev).

At the end of the detection procedure, for each observation we obtained a master source list, which provides the source counts, count rates and detection likelihoods for all sources in all the detection bands, together with their image position, sky position and overall detection likelihood.

Unfortunately, even using the maximum number of spline nodes (20), the fit performed in step 2 (see above) is not sufficiently flexible to model the local variations of the background. Therefore, it was necessary to correct each background map *pixel by pixel*, measuring the counts both in the *cheesed image* and in the background map itself applying the correction algorithm described in Baldi et al. (2002). All sources in the master list were checked against the corrected background maps and all their parameters calculated again. Then, for all the selected energy bands, we applied a minimum threshold of 8.5 on the corrected detection likelihoods $-\ln P$, corresponding to a probability $P(j) = 2 \cdot 10^{-4}$ that the source count number in the energy band j originate from a background fluctuation. This implies a contamination of at most 1 spurious source per energy band. The revised source master list was then filtered to include only sources with $-\ln P > 8.5$ in at least one of the selected energy bands and manually screened to reject residual false detections. The final master lists contain a total of 146 and 148 sources for the 3EG J0616–3310 and in the 3EG J1249–8330 error box, respectively.

3. X-ray Analysis

3.1. Global Statistics

In order to perform a full statistical analysis, we computed the number of detected sources in each of the 7 energy ranges, i.e. those ones with $P(j) < 2 \cdot 10^{-4}$ in the energy band j . Of

course, most of the sources are detected in several bands: in Table 2 we report, for each observation of both *EGRET* fields, the number of detected sources in each energy range and its percentage over the total (that is the total number of the sources which have been detected in at least one energy band).

We note that almost all sources are detected between 0.5 and 2 keV, with half of them also detected between 1 and 2 keV, while only very few sources are detected at very high or very low energies. The number of sources detected in each energy band is, in absolute terms, very different across the 8 pointings but, taking into account the uneven effective exposure times (as it is evident in the case of the observation of field 7, see Table 1), the relative number is constant, especially for those pointings associated with the same *EGRET* error box. However, we note that below 1 keV the fraction of detected sources is indeed lower for the 3EG J1249–8330 error box than for the 3EG J0616–3310 one, probably because of the difference in the neutral hydrogen column density, $\sim 10^{21}$ cm $^{-2}$ and $\sim 2.5 \cdot 10^{20}$ cm $^{-2}$, respectively.

3.2. Count Rate and S/N Distributions

The histograms of the source *count–rate* (*CR*) distribution for the two coarse soft (0.5–2 keV) and hard (2–10 keV) energy bands are shown in Figure 3, for the single pointings of the two *EGRET* error boxes. Since the number of sources per *CR* bin decreases below the peak *CR*, we deduce that our sample becomes incomplete for lower *CR* values (the same approach was used by Zickgraf et al. (1997)). Therefore, we assume the *CR* peak values as our completeness limit. In all the pointings of the 3EG J0616–3310 error box, the source count–rate distributions in the low (0.5–2 keV) energy range are pretty similar, with peaks at $\log CR \approx -2.6$; on the other hand, there are some differences among the distributions of 3EG J1249–8330. The marginal differences in the count–rate distributions between the pointings of the two *EGRET* sources are an obvious effect of the larger hydrogen column density. On the other hand, the count–rate distributions in the high energy range (2–10 keV) are significantly different, with peaks at $\log CR \leq -3$.

The histograms of the source *signal–noise* (*S/N*) distribution in the whole energy range are reported in Figure 4 for all the pointings of the two *EGRET* error boxes. The two distributions peak between 4.5 and 5.5, with only a few sources at $S/N \geq 10$.

3.3. Source Hardness Ratios Distribution

Since the count statistics (usually a few tens of photons) of the detected sources is too low to produce significant spectra, we have performed a qualitative spectral analysis using the *CR*

measured in the seven energy ranges defined above to compute four different *Hardness Ratios* (*HRs*):

$$HR1 = [CR(0.5–1) - CR(0.3–0.5)]/[CR(0.5–1) + CR(0.3–0.5)]$$

$$HR2 = [CR(1–2) - CR(0.5–1)]/[CR(1–2) + CR(0.5–1)]$$

$$HR3 = [CR(2–4.5) - CR(0.5–2)]/[CR(2–4.5) + CR(0.5–2)]$$

$$HR4 = [CR(4.5–10) - CR(2–4.5)]/[CR(4.5–10) + CR(2–4.5)]$$

The histograms of the *HRs* distributions are shown in Figure 5 for the combined pointings of both *EGRET* error boxes. Most sources have $HR1 \geq 0.5$, $-0.1 < HR2 < +0.4$, $HR3 < -0.5$ and $HR4 \simeq -1$. These results, together with those of §3.2 based on the count distributions, suggest that, for both error boxes, the source population is characterised on average by rather soft spectra.

To obtain a further indication on the sources spectra, we compared the measured *HRs* with the expected ones computed for two different template spectral models (Giacconi et al. 2001; Barcons et al. 2002), namely: a thermal *bremsstrahlung*, with temperatures *kT* increasing from 0.5 (left) to 5 keV (right), and a *power–law*, with photon indexes Γ increasing from 1 (right) to 2.5 (left). In such a way we could identify the spectral model more appropriate for a given source and tentatively assign its most likely spectral parameters. The values of the expected *HRs* are overplotted as vertical bars in Figure 5. As can be seen, the distributions are compatible with a rather wide range of temperatures and photon indexes, thus suggesting that we are indeed sampling different types of sources. This conclusion is not surprising, since the two areas are at medium galactic latitude and therefore are expected to contain both galactic and extragalactic X-ray sources.

3.4. Sky Coverage and $\log N$ – $\log S$

In order to compute the source fluxes, we assumed a template *power–law* spectrum with average photon index $\Gamma = 1.7$. For each pointing, we estimated the hydrogen column density N_H (see Table 1) from the relation $N_H = 4.8 \times 10^{21} \times E(B - V)$ cm $^{-2}$ (Zombeck 1990) using the average colour excess $E(B - V)$ derived from the dust maps developed by Schlegel et al. (1998). Following the procedure used by Baldi et al. (2002), *count–rate–to–flux* conversion factors (*CF*) were computed for the *PN* and the *MOS* cameras individually using their updated response matrices and then combined with the effective exposure times of each pointing to derive the *total* conversion factor *CF*. For each pointing and for each energy range we used the exposure maps of each camera and the background map of the merged image to compute the *flux limit* map, which gives, at each celestial coordinate, the minimum flux of a source in order to be detected with a probability $P = 2 \cdot 10^{-4}$ (Baldi et al. 2002). Then, we used the flux limit maps to derive the total sky coverage of both *EGRET* error boxes. These are shown in Figure 6, in the two standard *soft* (0.5–2 keV) and *hard* (2–10 keV) energy bands.

Figure 7 shows the cumulative $\log N$ – $\log S$ distributions of the sources detected in the two energy ranges 0.5–2 and 2–10 keV. For comparison, we overplotted the lower and upper

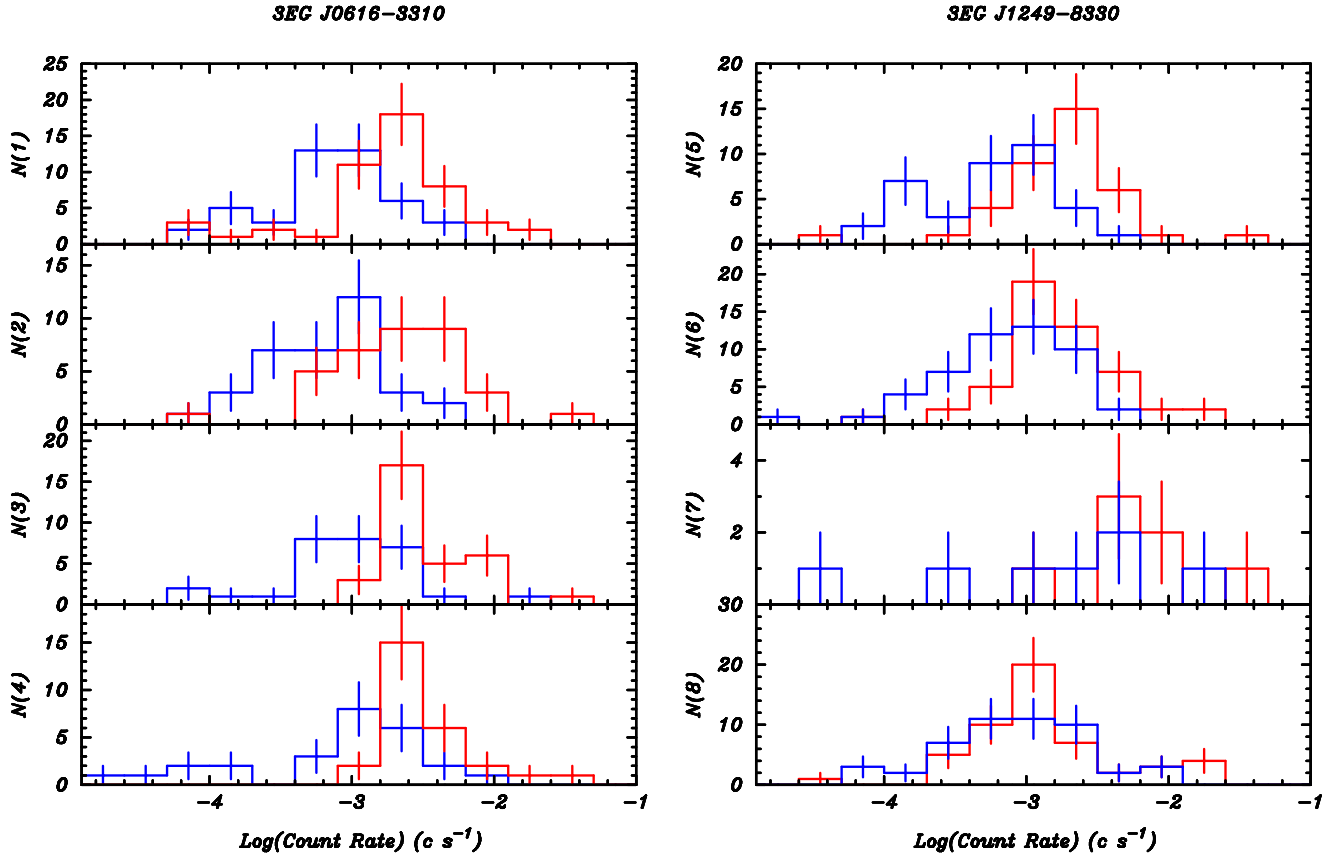


Fig. 3. Histograms of the source count–rate distributions for each *EPIC* pointing of the error box of 3EG J0616–3310 (left, $N1$ – $N4$) and 3EG J1249–8330 (right, $N5$ – $N8$), in the energy ranges 0.5–2 keV (red line) and 2–10 keV (blue line). For observation 7 the distribution peaks at higher count rate ($\log CR = -2.35$) due to the shorter effective exposure time.

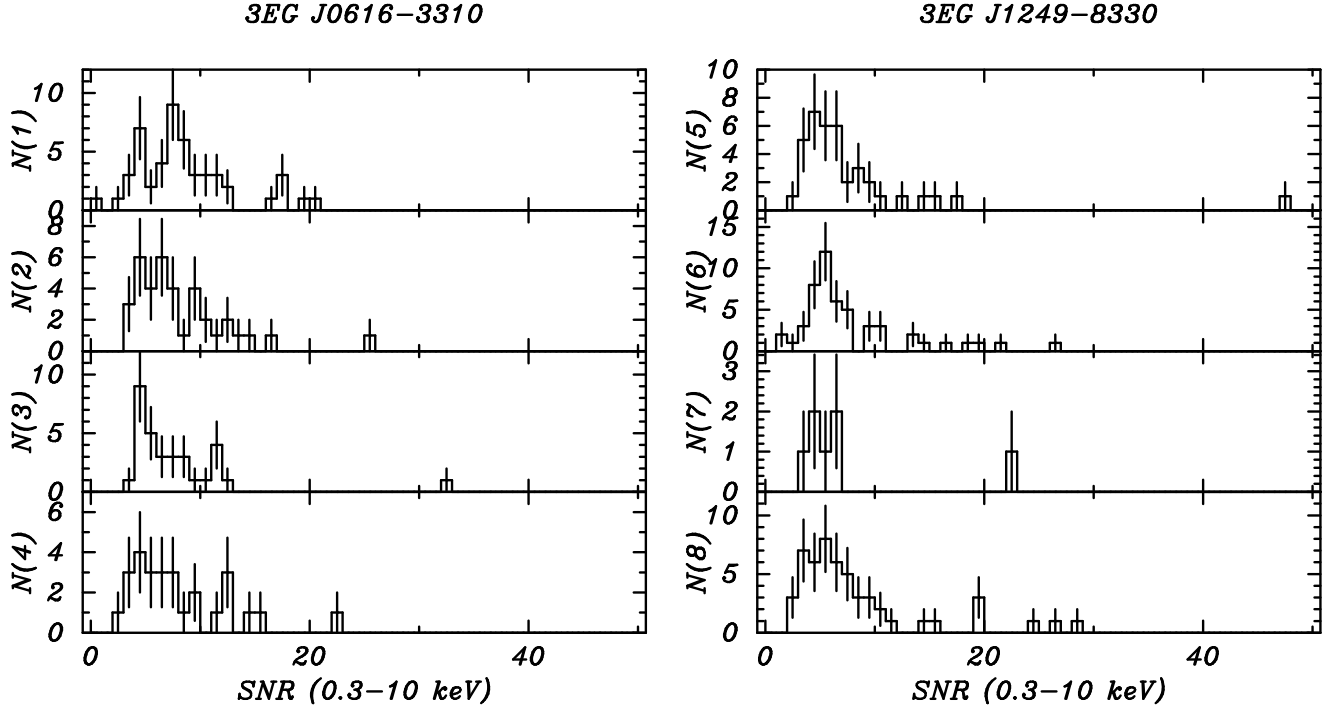
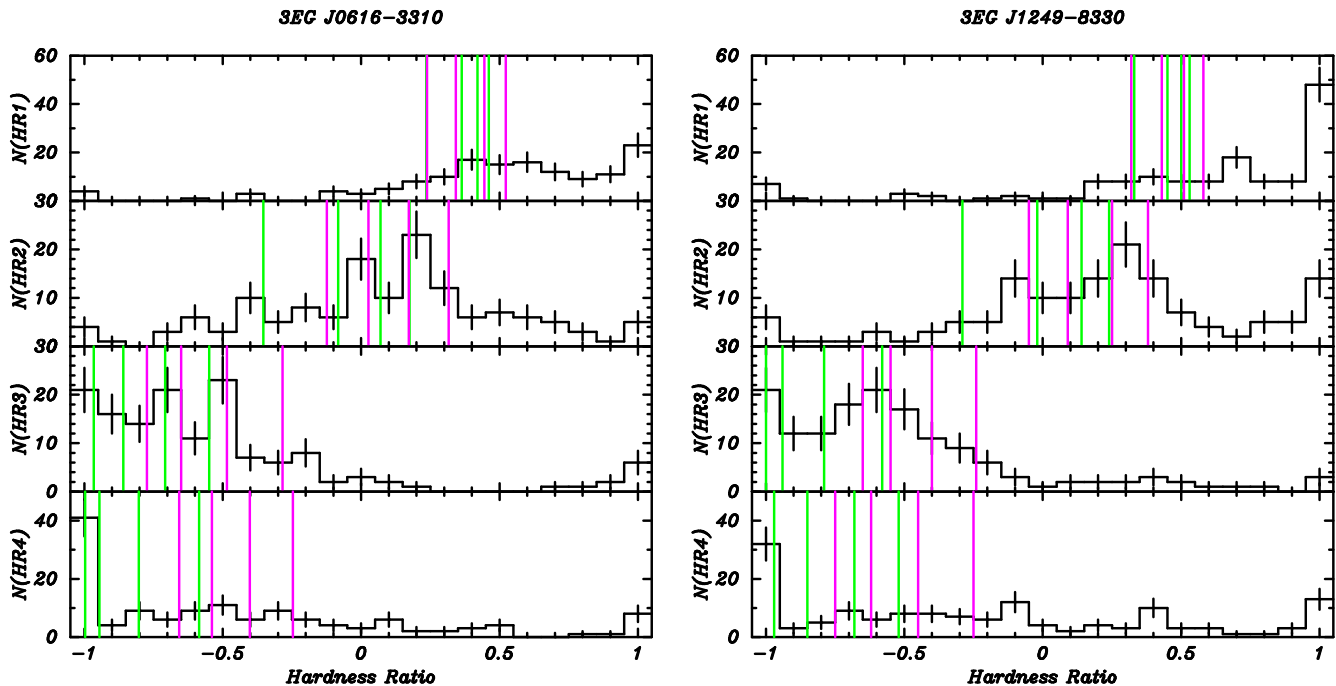


Fig. 4. Histogram of the source S/N distribution for the 3EG J0616-3310 (left, $N1$ – $N4$) and 3EG J1249–8330 (right, $N5$ – $N8$) fields.

Table 2. X-ray sources detected in each energy range.

Range (keV)	0.5–2	2–10	0.3–0.5	0.5–1	1–2	2–4.5	4.5–10	Total
Field ID	N(%)	N(%)	N(%)	N(%)	N(%)	N(%)	N(%)	N
1	37 (74)	18 (36)	11 (22)	25 (50)	29 (58)	18 (36)	1 (2)	50
2	28 (75.7)	8 (21.6)	6 (16.2)	23 (62.2)	17 (45.9)	11 (29.7)	0 (0)	37
3	28 (87.5)	6 (18.7)	7 (21.9)	14 (43.7)	21 (65.6)	7 (21.9)	2 (6.2)	32
4	26 (96.3)	9 (33.3)	4 (14.8)	11 (40.7)	14 (51.9)	11 (40.7)	1 (3.7)	27
3EG J0616–3310	119 (81.5)	41 (28.1)	28 (19.2)	73 (50)	81 (55.5)	47 (32.2)	4 (2.7)	146
5	32 (84.2)	8 (21.1)	4 (10.5)	10 (26.3)	20 (52.6)	6 (15.8)	1 (2.6)	38
6	37 (72.5)	13 (25.5)	6 (11.8)	16 (31.4)	29 (56.9)	13 (25.5)	4 (7.8)	51
7	6 (85.7)	2 (28.6)	1 (14.3)	2 (28.6)	2 (28.6)	1 (14.3)	1 (14.3)	7
8	44 (84.6)	19 (36.5)	3 (5.8)	15 (28.8)	26 (50)	16 (30.8)	3 (5.8)	52
3EG J1249–8330	119 (80.4)	42 (28.4)	14 (9.5)	43 (29.1)	77 (52)	36 (24.3)	8 (5.4)	148

**Fig. 5.** Histograms of the HR distributions for sources in the 3EG J0616-3310 (left) and 3EG J1249-8330 (right) error boxes. Green bars indicate the expected HR s computed for *thermal bremsstrahlung* spectra with $kT = 0.5, 1, 2$ and 5 keV (from left to right). Magenta bars indicate the expected HR s computed for *power-law* spectra with $\Gamma = 1, 1.5, 2$ and 2.5 (from right to left).

limits of the same distributions as measured at high galactic latitude, where only extragalactic sources are expected to contribute (Baldi et al. 2002). In both cases our source density is above the upper limit of the high latitude distribution, especially in the soft energy band and at low fluxes. This result points to a significant excess of galactic sources, whose fraction is larger at softer energies and lower fluxes.

4. Optical Observations

In order to search for the optical counterparts of our X-ray sources, we used the *Wide Field Imager* (*WFI*)¹ mounted at the 2.2m ESO/MPG telescope at La Silla (Chile), where we collected data under programme ID 68.D-0478. The *WFI* is a wide field mosaic camera, composed of eight 2048×4096 pixel CCDs, with a scale of $0''.238/\text{pixel}$ and a full field of view

of $33''.7 \times 32''.7$. As it matches very well the diameter of *XMM-Newton/EPIC* field of view (~ 30 arcmin), *WFI* can provide a complete coverage of the targets' area with a minimum number of pointings. Observations in the filters $U(877)$, $B(842)$, $V(843)$, $R(844)$ and $I(845)$ ² were requested in order to maximize the optical spectral coverage and to optimise the objects classification in the colour space. To compensate for the interchip gaps, for each passband the pointings were split in sequences of five dithered exposures with shifts of $35''$ and $21''$ in RA and DEC, respectively. Observations were performed in Service Mode between December 2001 and March 2002. Unfortunately, bad weather conditions as well as scheduling problems resulted in a highly incomplete and inhomogeneous dataset and in a data quality in some cases far from optimal. In

¹ <http://www.ls.eso.org/lasilla/sciops/2p2/E2p2M/WFI/>

² <http://www.ls.eso.org/lasilla/sciops/2p2/E2p2M/WFI/filters/>

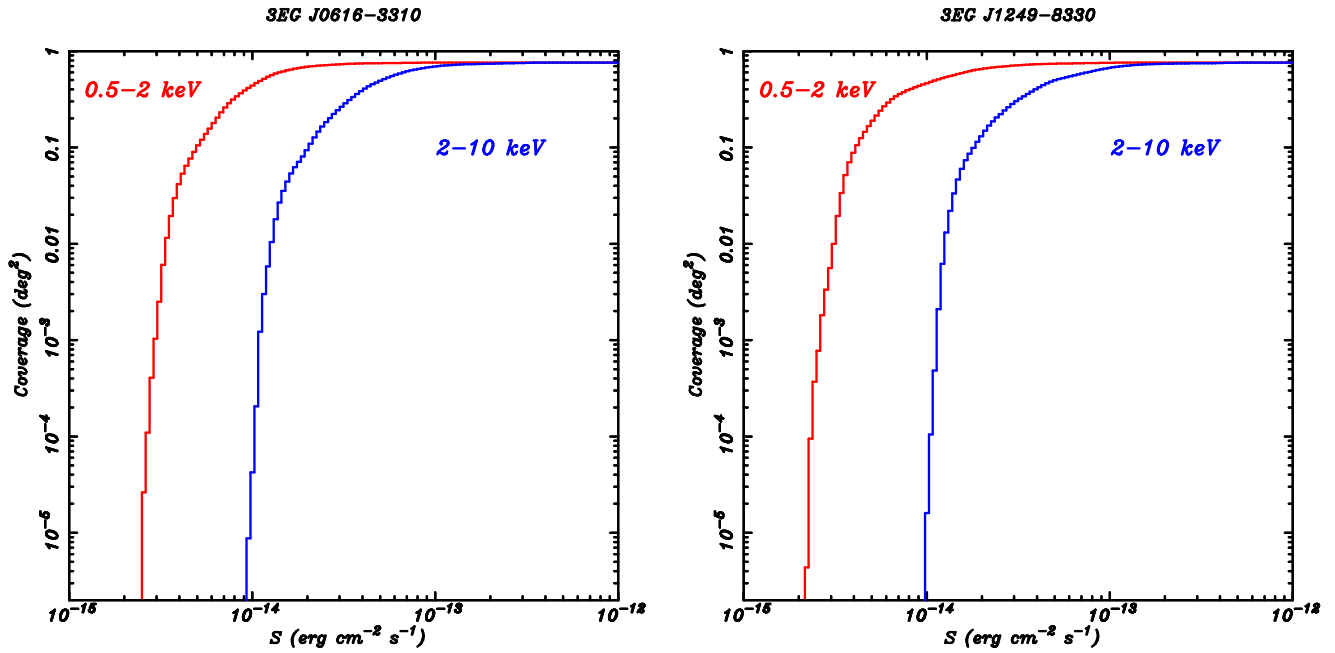


Fig. 6. The total sky coverage of the EPIC observations of the 3EG J0616–3310 (left) and 3EG J1249–8330 (right) error boxes, in the energy bands 0.5–2 keV (red line) and 2–10 keV (blue line).

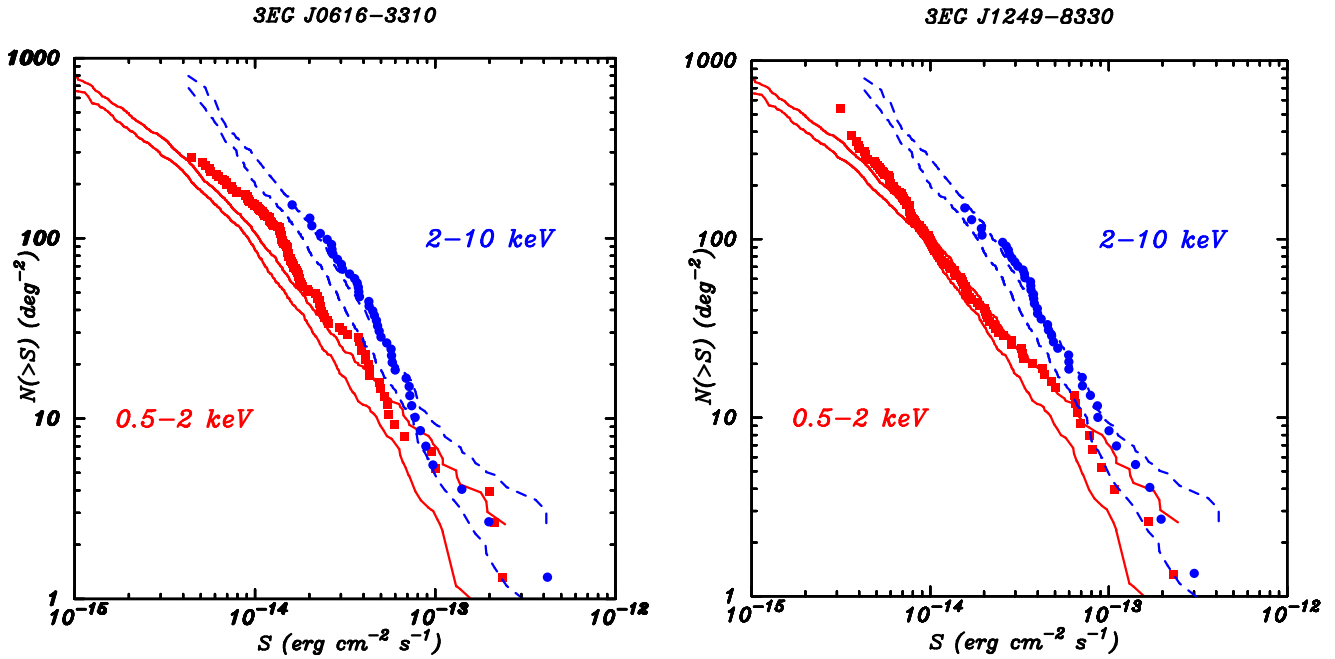


Fig. 7. Cumulative logN–logS distribution of the sources detected in the EPIC observations of the 3EG J0616–3310 (left) and 3EG J1249–8330 (right) error boxes, in the energy bands 0.5–2 keV (red squares) and 2–10 keV (blue dots). For comparison, in both diagrams we also show the lower and upper limits of the high latitude logN–logS in the energy ranges 0.5–2 keV (red solid lines) and 2–10 keV (blue dashed lines).

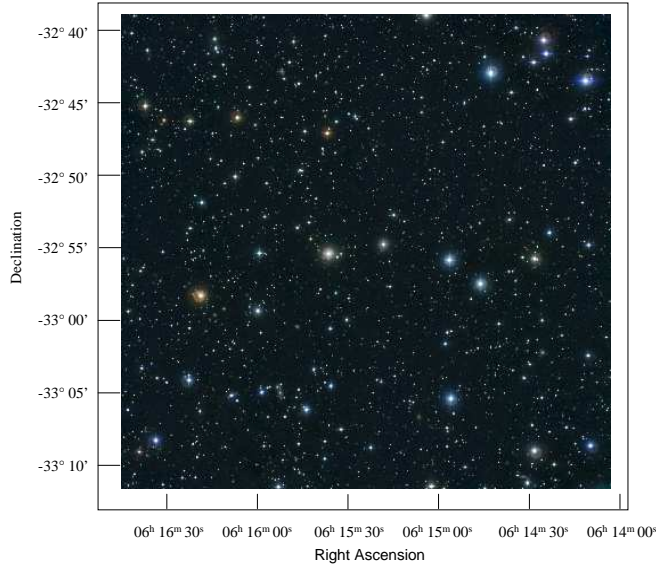
particular, only four of the eight *XMM-Newton* fields were covered by the *WFI*, i.e. fields 2, 3 and 4 of the 3EG J0616–3310 error box and field 8 of the 3EG J1249–8330 error box (see Table 3 for a summary of the observations).

4.1. Data Reduction

The data reduction was performed with a pre-release version of *THELI*, a fully automatic pipeline for the reduction of optical and near-IR imaging data obtained with single- or multi-chip cameras. A detailed description of this pipeline and the

Table 3. Summary of the optical observations performed by the *Wide Field Imager* of the 2.2m MPG/ESO telescope at La Silla.

Date dd.mm.yyyy	Field ID	Filter Name	Number of Frames	Exposure Time (s)	Average Seeing	Average Airmass
06.03.2002	2	U	5	2500.0	1.20	1.15
06.03.2002	2	B	5	1500.0	1.18	1.28
10.02.2002	2	V	5	2000.0	1.12	1.30
05.03.2002	3	U	5	2500.0	1.07	1.14
10.02.2002	3	V	5	2000.0	1.29	1.16
05.03.2002	3	R	5	2000.0	0.82	1.05
08.03.2002	3	I	13	3250.0	1.01	1.18
05.03.2002	4	U	5	2500.0	1.14	1.30
12.12.2001	4	B	5	1500.0	1.09	1.05
12.12.2001	4	V	5	2000.0	1.09	1.01
12.12.2001	4	R	5	2000.0	1.00	1.11
10.02.2002	8	B	1	500.0	1.69	1.70
11.02.2002	8	V	4	2000.0	1.64	1.73

**Fig. 8.** Composite *BVR* image (*B* = blue; *V* = green; *R* = red) of field 4 taken with *WFI* at the ESO/MPG 2.2m telescope.

algorithms used can be found in Schirmer et al. (2003) and in Erben et al. (2005). Here we describe only the steps relevant for the the *WFI* multi-chip detector, such as astrometric and photometric calibration, image dedithering and coaddition. All pre-processing steps (debiasing, flat fielding, superflatting etc.) are similar to those performed with single chip cameras.

The astrometric solution was performed in several steps. First, for each CCD chip pre-processed image we run the *SExtractor* object detection algorithm (Bertin & Arnouts 1996) to generate a catalogue which contained high S/N (DETECT_MINAREA = 10, DETECT_THRESH = 10) non saturated objects. Objects classified as stars according to the *SExtractor* parameters were then matched, using the crude *WFI* pointing astrometric solution, with the USNO-A2 astrometric catalogue which has a nominal intrinsic absolute astrometric accuracy of $\sim 0''.25^3$.

³ http://ad.usno.navy.mil/star/star_cats_rec.html

Thereafter, for each chip all the detected objects within the overlapping regions of the dithering pattern were cross-matched and the results were piped into two χ^2 minimisation routines. The first one fits two dimensional third order polynomials to the optical distortion of each chip, whereas the second one determines the relative photometric zeropoint with respect to all other chips. The final image coaddition was performed chip by chip using as a reference the computed chip distortion maps and the relative chip flux normalization.

Before performing this step, individual weight maps were created for each exposure, based on normalized skyflats. The detection of defect pixels was performed on the individual chips by means of *SExtractor* and *Eye*⁴. Those pixels were then set to zero in the weight map. Thereafter, the sky background was modelled and subtracted, and the chips were resampled and coadded by means of the *IRAF EISdrizzle* routine, using the weight maps created previously. The registration of the individual chips was accurate within $\sim 1/10$ th of a pixel ($0''.02$), so that we did not introduce any artificial decrease of the image quality. After mosaicing, the final image was associated with its corresponding weight map, containing information on how long each pixel has been exposed. This is particular useful since, due to the dithering pattern and the gaps between the CCDs, the total exposure time in the coadded image was highly inhomogeneous. Using the method described above, we could assign to the coadded mosaic a consistent global astrometric solution accurate within $0''.3$ and a relative photometric zero-point constant within ~ 0.05 mag.

Figure 8 shows as example a composite *WFI* image of field 4 obtained after co-adding the single-passband *BVR* reduced images.

4.2. Optical Catalogues

Source extraction was performed by *SExtractor* on the final co-added images using the previously created weight maps to properly account for the varying depths of the mosaics. Our parameter combination (DETECT_THRESH = 2.0 and

⁴ <http://terapix.iap.fr>

Table 4. Limiting magnitudes (3σ) of our multiband optical-to-IR photometry. $UBVRI$ values are derived either from the *WFI* observations or, when not available, from the *GSC-2.3* B_J, F, N equivalent (in *italics*). JHK values are taken from *2MASS*. An hyphen indicates that no measurements are available. The last column lists the total number of objects per pointing after matching over all the passbands.

Field ID	U	B	V	R	I	J	H	K	N
1	-	23.0	-	22.0	19.5	15.8	15.1	14.3	5688
2	23.9	25.1	24.7	22.0	19.5	15.8	15.1	14.3	20837
3	24.5	23.0	24.7	24.6	23.3	15.8	15.1	14.3	32202
4	23.8	25.1	24.7	24.5	19.5	15.8	15.1	14.3	34093
5	-	23.0	-	22.0	19.5	15.8	15.1	14.3	11329
6	-	23.0	-	22.0	19.5	15.8	15.1	14.3	7423
7	-	23.0	-	22.0	19.5	15.8	15.1	14.3	6820
8	-	24.5	24.3	22.0	19.5	15.8	15.1	14.3	15578

`DETECT_MINAREA` = 8 pixels) turned out to be the optimal one as it maximizes the number of detections yielding little contamination by spurious objects, located around saturated stars. For uniformity reasons, we applied the same values for all catalogues. Even though the detection threshold is admittedly low, we decided to use this value in order to provide candidate optical counterparts for as many X-ray sources as possible. The extracted catalogues were overlayed on the images and the counterparts were visually inspected. The percentage of spurious objects at the images' borders was less than 1%.

Since a very high photometric accuracy is not critical for the purpose of this work, default zeropoints provided by the *WFI* science operation team⁵ were used for the photometric calibration. The adopted zeropoints (in the *Vega* magnitude system) are 21.96, 24.53, 24.12, 24.43 and 23.37 for the U , B , V , R , and I filters, respectively.

Since the optical coverage of the two fields performed with the *WFI* is not complete, both in terms of sky and passband (see Table 3), we have complemented our dataset using a, yet unpublished, version of the *Guide Star Catalogue 2* (*GSC-2.3*) which provides photometry in the B_J , F and N passbands, overlapping the Johnson's B , R , and I^6 , down to 3σ limiting magnitudes of $B_J \sim 23$, $F \sim 22$ and $N \sim 19.5$, with average errors of ~ 0.25 (at $B_J \sim 20$). In addition, to extend our passband coverage to the near-IR, we have used the *Two Micron All Sky Survey* (*2MASS*) catalogue (Cutri et al. 2003), which provides photometry in the J (1.25μ), H (1.65μ) and K (2.65μ) passbands down to limiting magnitudes of 15.8, 15.1 and 14.3, respectively.

We then cross-correlated all the available catalogues (*WFI*, *GSC-2.3* and *2MASS*) to produce master *optical-to-IR* catalogues for each of the eight fields. The four *WFI* catalogues (relative to fields 2, 3, 4 and 8) were cross-correlated in turn with both the *2MASS* Point Source and Extended Source Catalogues through the *Gator* www interface⁷. Then, the two output catalogues were merged and cross-correlated with the *GSC-2.3*. For the remaining fields, we extracted the corresponding object catalogues from the *GSC-2.3* through the

same interface and we cross-correlated them with both the *2MASS* Point Source and Extended Source Catalogues using *Gator*. In all cases, we used a fixed cross-correlation radius of 1 arcsec which largely accounts for the uncertainty in the absolute astrometric calibrations of the *WFI* catalogues ($\approx 0.^{\prime}3$), of the *GSC-2.3* ($\approx 0.^{\prime}35^8$) and *2MASS* ($\approx 0.^{\prime}25^9$). The final colour coverage for each of the eight fields is summarized in Table 4, together with the estimated limiting magnitude in each passband and the total number of single objects extracted from the optical-to-IR master catalogues. The same catalogues are also used for a multi-colour analysis aimed at the characterization of the stellar/galactic populations in the fields (Hatziminaoglou et al., in preparation).

5. Cross-correlations

5.1. X-rays vs. Optical Catalogues

Since the absolute coordinate accuracy of *XMM-Newton* is $\sim 5''$ (Kirsch et al. 2004), i.e. a factor 10 worse than the astrometric accuracy ($\leq 0.^{\prime}5$) of our optical/IR data, we first tried to improve the accuracy of the X-ray coordinates. After overlaying the X-ray positions on the *Digital Sky Survey* images, we found few X-ray sources which could be confidently associated with a single bright optical object and we assumed the optical positions as the true ones. Then, using the *IRAF* task *geomap*, we calculated the correction to be applied to the X-ray coordinates (value always $\leq 2''$) and we applied it to all the remaining X-ray sources using the *IRAF* task *geoxtraj*. In the following, we decided to use a conservative value of $5''$ (i.e. ~ 3 times our astrometric correction) for the cross-correlation radius.

In Table 5 we report, for each *XMM-Newton* field, the number of X-ray sources with and without candidate optical/IR counterparts, as well as the total number of candidate counterparts. It is evident that the results of the cross-correlations are significantly different for the different fields, depending on the varying limiting magnitude of the optical coverage (see Table 4). For instance, for most X-ray sources of fields 1 and 5–7 we found no candidate counterpart within $5''$, owing to the limiting flux of *GSC-2.3* which is, on average, a factor 6

⁵ <http://www.ls.eso.org/lailla/sciops/2p2/E2p2M/WFI/zeropoints/>

⁶ see <http://www.stsci.edu/> for a more detailed description of the *GSC-2* photometric system

⁷ <http://irsa.ipac.caltech.edu/applications/Gator/>

⁸ <http://www-gsss.stsci.edu/gsc/gsc2/GSC2home.htm>

⁹ <http://spider.ipac.caltech.edu/staff/hlm/2mass/overv/overv.html>

Table 5. Results of the cross-correlations between the list of X-ray sources and the optical/IR master catalogues. For all fields, the total number of candidate counterparts is larger than those of the X-ray sources because of multiple matches.

Field ID	Detected Sources	X-ray sources with no counterpart	X-ray sources with counterpart	Candidate Counterparts	Reliability (1-P)
1	50	27	23	26	84 %
2	37	7	30	46	76 %
3	32	7	25	41	82 %
4	27	3	24	40	70 %
Total	146	44	102	153	-
5	38	18	20	21	71 %
6	51	34	17	19	80 %
7	7	5	2	2	81 %
8	52	24	28	37	76 %
Total	148	81	67	79	-

shallower in flux than the *WFI* catalogues. Indeed, the fraction of X-ray sources without candidate counterparts decreases drastically for fields 2–4. This is particularly true for field 4, probably due to its short X-ray effective exposure time (see Table 1) which results in the detection of only relatively bright X-ray sources, with presumably brighter optical counterparts. Conversely, the longer X-ray effective exposure time of field 8 results in the detection of fainter X-ray sources, presumably characterized by fainter optical counterparts.

The cross-correlation between X-ray and optical catalogues is obviously affected by spurious matches. In order to estimate it, we computed from the optical/IR master catalogues the total number of objects within the areas encompassed by each *XMM-Newton* fields. Then, we used the relation $P = 1 - e^{-\pi r^2 \mu}$, where r is the X-ray error circle radius (5'') and μ is the surface density of the optical objects (per square degree), to obtain the chance coincidence probability between an X-ray and an optical object (Severgnini et al. 2005). By assuming an X-ray error circle of 5'', for each observation we estimated the probability P to vary between 16 and 30 % over all the eight fields (see Table 5), which means that, at our limiting magnitudes, contamination effects cannot be ignored in the evaluation of the candidate counterparts.

5.2. X-rays vs. Radio catalogues

All X-ray sources were also cross-correlated with radio catalogues, namely:

- The *Parkes Radio Source* catalogue (PKSCAT90), which includes 8264 radio object at $\delta < +27^\circ$ (Wright & Otrupcek 1990)
- The *Parkes-MIT-NRAO* source catalogue (PMN) for both the Southern and the Zenith surveys: the first one reports 23277 radio sources at $-87.5^\circ < \delta < -37^\circ$ (Wright et al. 1994); the second one includes 2400 sources with $-37^\circ < \delta < -29^\circ$ (Wright et al. 1996)
- The *NRAO VLA Sky Survey* catalogue (NVSS), which has almost 2 million sources at $\delta > -40^\circ$ (Condon et al. 1998)

We obtained a positional coincidence with a NVSS object for just 3 X-ray sources detected in field 1: NVSS 5228 for

source XMMU J061759.1-325850, NVSS 5190/MRC 0616-329 for source XMMU J061756.6-324735 and NVSS 4464 for source XMMU J061721.5-330110. Of these, only source XMMU J061756.6-324735 has a candidate optical counterpart. Moreover, a marginal spatial correlation with NVSS 2588 was obtained for source XMMU J061546.9-333347 of field 3, which has no candidate optical counterpart. For all the other X-ray sources no candidate radio counterpart was found within the 5'' radius error circles.

6. X-ray/Optical Analysis

6.1. The X-ray-to-optical flux ratio Classification Scheme

Observations performed with several X-ray missions have shown that different classes of X-ray emitters have different, rather narrow, ranges of X-ray-to-optical flux ratios f_X/f_{opt} (Stocke et al. 1991; Krautter et al. 1999). In particular, such a ratio is very high (i.e. ≥ 1000) for INSs while it is lower for all the other classes of X-ray sources, with no, or small, overlapping between the respective range of values. Therefore, we can use this parameter in order to reject or retain an X-ray source as a candidate INS. For the f_X/f_{opt} values we considered the results of the *Hamburg/ROSAT All Sky Survey* (Zickgraf et al. 2003), which provides the typical range of values for each class of celestial sources, as a ‘reference’ classification scheme. We considered the same objects classes, i.e. white dwarfs (WD), cataclysmic variables (CV), galaxies (G), cluster of galaxies (CG) and active galactic nuclei (AGN). Moreover, we considered stars as a single class (S). In the *Hamburg/RASS* the X-ray flux is calculated in the *ROSAT* energy range 0.1–2.4 keV, assuming a ‘typical’ spectral shape for each class of sources, while the optical flux is based on their B magnitude.

In our case we calculated the source flux in the *XMM-Newton* energy range 0.3–10 keV, and assumed a common emission model for all sources (a *power-law* with photon index $\Gamma = 1.7$ and galactic column density). Moreover, as shown in the previous section, the passband coverage of the *WFI* observations is incomplete, with only V available in all fields (see Table 4) for 90 candidate counterparts (~ 70 % of the total).

Table 6. Range of the expected f_X/f_{opt} flux ratios (min/max value in logarithmic units) for the different object classes and *EPIC* fields. The X-ray fluxes refer to the full *XMM*-Newton energy range (0.3–10 keV), while the optical fluxes refer to the Johnson’s B (top) and V (middle) bands and to the B_J band (bottom). For each source class the slight differences in the f_X/f_{opt} values are due to the different N_{H} of the various *EPIC* fields, which affects the count–rate–to–flux conversion factor.

Field ID	Stars min/max	WDs min/max	CVs min/max	Galaxies min/max	Clusters min/max	AGN min/max
1	-3.90/+0.50	+1.00/+2.70	-1.02/+1.42	-0.54/+1.83	+0.38/+2.11	+0.25/+1.72
2	-3.91/+0.49	+0.99/+2.69	-1.02/+1.41	-0.54/+1.83	+0.37/+2.10	+0.26/+1.73
3	-3.93/+0.47	+0.95/+2.65	-1.04/+1.39	-0.55/+1.82	+0.38/+2.11	+0.23/+1.70
4	-3.94/+0.45	+0.89/+2.60	-1.06/+1.38	-0.56/+1.81	+0.38/+2.11	+0.22/+1.69
5	-3.80/+0.60	+1.11/+2.81	-0.91/+1.52	-0.44/+1.94	+0.48/+2.21	+0.35/+1.82
6	-3.81/+0.59	+1.10/+2.80	-0.92/+1.51	-0.45/+1.92	+0.46/+2.19	+0.34/+1.81
7	-3.84/+0.56	+1.04/+2.74	-0.96/+1.48	-0.47/+1.91	+0.46/+2.20	+0.32/+1.78
8	-3.78/+0.62	+1.12/+2.82	-0.90/+1.54	-0.42/+1.95	+0.49/+2.22	+0.37/+1.84

Field ID	Stars min/max	WDs min/max	CVs min/max	Galaxies min/max	Clusters min/max	AGN min/max
1	-4.33/+0.87	+0.65/+3.11	-1.54/+1.63	-0.89/+2.04	+0.07/+2.00	-0.10/+2.25
2	-4.33/+0.86	+0.64/+3.10	-1.55/+1.62	-0.89/+2.04	+0.06/+2.00	-0.09/+2.26
3	-4.35/+0.84	+0.60/+3.06	-1.57/+1.60	-0.90/+2.03	+0.07/+2.00	-0.12/+2.23
4	-4.37/+0.83	+0.55/+3.01	-1.58/+1.59	-0.90/+2.02	+0.07/+2.00	-0.13/+2.22
5	-4.22/+0.97	+0.76/+3.22	-1.44/+1.73	-0.78/+2.15	+0.17/+2.10	+0.01/+2.36
6	-4.24/+0.96	+0.76/+3.22	-1.45/+1.72	-0.80/+2.13	+0.15/+2.08	-0.01/+2.34
7	-4.27/+0.93	+0.69/+3.15	-1.48/+1.69	-0.81/+2.12	+0.16/+2.09	-0.03/+2.32
8	-4.21/+0.99	+0.78/+3.23	-1.42/+1.75	-0.77/+2.16	+0.18/+2.11	+0.02/+2.37

Field ID	Stars min/max	WDs min/max	CVs min/max	Galaxies min/max	Clusters min/max	AGN min/max
1	-4.19/+0.43	+0.74/+2.65	-1.33/+1.31	-0.81/+1.72	+0.13/+1.91	-0.02/+1.70
2	-4.19/+0.43	+0.73/+2.64	-1.33/+1.30	-0.81/+1.72	+0.12/+1.91	+0.00/+1.71
3	-4.21/+0.41	+0.69/+2.59	-1.35/+1.28	-0.82/+1.71	+0.13/+1.91	-0.04/+1.68
4	-4.23/+0.39	+0.64/+2.55	-1.37/+1.27	-0.82/+1.71	+0.13/+1.91	-0.05/+1.67
5	-4.08/+0.54	+0.85/+2.76	-1.22/+1.41	-0.70/+1.83	+0.23/+2.01	+0.09/+1.81
6	-4.09/+0.53	+0.85/+2.75	-1.24/+1.40	-0.72/+1.81	+0.21/+2.00	+0.07/+1.79
7	-4.13/+0.49	+0.78/+2.68	-1.27/+1.37	-0.73/+1.80	+0.21/+2.00	+0.05/+1.77
8	-4.07/+0.55	+0.87/+2.77	-1.21/+1.43	-0.69/+1.84	+0.24/+2.03	+0.10/+1.82

However, for fields 2 and 4 the B band limiting is deeper than the V band one probably owing to the large QE of the detector. Therefore, to define our classification scheme, we decided to compute the measured f_X/f_{opt} ratio for both the B and V bands, while, for candidate counterparts with only *GSC*–2.3 photometry, the f_X/f_{opt} ratio was computed from the B_J magnitude.

Moreover, for each class of sources we had to correct the f_X/f_{opt} ratio found in the *Hamburg/RASS* by accounting for the *XMM–Newton* detection band, the different assumed spectral models and the different optical filter. To this aim, we have devised a procedure which is described in the Appendix A. The computed f_X/f_{opt} ranges, relative to the B , V and B_J passbands, for the different classes of X-ray sources are listed in Table 6. The reported values are in rough agreement with the results obtained by Krautter et al. (1999) and by Zickgraf et al. (2003), except for the WD class. In this case, the discrepancy is due to the correction applied to the *Hamburg–RASS* flux ratio in order to obtain the corresponding *XMM–Newton* one. In fact, in the first case a very soft blackbody spectrum ($T = 50000$ K) was

adopted, while we consider a rather hard ($\Gamma = 1.7$), less realistic power–law spectrum; moreover, the *ROSAT* energy range (0.1–2.4 keV) is very suitable for the WD detection, which is not the case for the considered *XMM–Newton* one (0.3–10 keV). Both the items imply that, if the count rate of a WD is high enough to be detected by *XMM–Newton*, we would assign it an unrealistic large flux.

6.2. Evaluation of the X-ray–to–optical flux ratios

The values of X–ray–to–optical flux ratios f_X/f_{opt} for all X–ray sources are shown in Figure 9 for all the available optical passbands. When a single X–ray source has more than one candidate counterpart, we report the f_X/f_{opt} value computed for each candidate counterpart. In the case of X–ray sources with no optical counterpart, we estimated the lower limits on the f_X/f_{opt} ratio from the limiting magnitudes of the different fields (see table 4). Thus, we assumed limiting magnitudes $V = 24.7$ for fields 2–4 and $V = 24.3$ for field 8 while for fields 1 and 5–7 we assumed a limiting magnitude of $B_J = 23$.

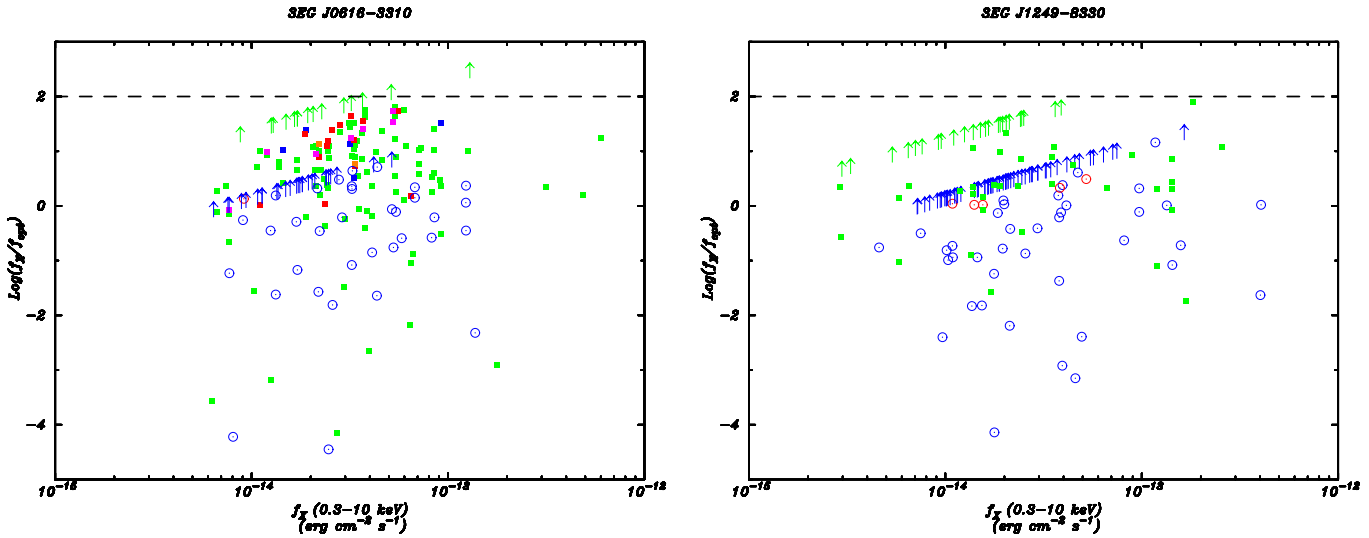


Fig. 9. X-ray-to-optical flux ratios f_X/f_{opt} for the X-ray sources detected in the 3EG J0616–3310 (left) and 3EG J1249–8330 (right) fields plotted as a function of the X-ray flux. Different colours refer to magnitudes computed in different bands i.e. V (green), B , B_J (blue), R , R_F (red). In case of multiple optical counterparts for a single X-ray source, the f_X/f_{opt} value of each candidate counterpart is shown. Vertical arrows indicate the lower limit on f_X/f_{opt} for sources with no candidate optical counterpart down to $B_J = 23$, $V = 24.7$ (left) and $V = 24.3$ (right). The dashed lines at $\log(f_X/f_{\text{opt}}) = 2$ represent the threshold level for a source to be considered as a possible INS candidate.

The systematic optical identification of all X-ray sources listed in our catalogue will be presented in detail in a future paper (La Palombara et al., in preparation). However, on the basis of our X-ray-to-optical flux ratio classification scheme (see Table 6), it is very likely that sources with $\log(f_X/f_{\text{opt}}) < -1.5$ are stars. The maximum value measured for $\log(f_X/f_{\text{opt}})$ is ~ 1.9 for sources with a *WFI* candidate counterpart (fields 2–4 and 8) and ~ 1.2 for those with a candidate *GSC* counterpart (pontings 1 and 5–7). These values are fully compatible with those typical of various classes of X-ray sources, especially the extragalactic ones (AGN or cluster of galaxies). Therefore, if we assume that all the above X-ray sources are indeed identified with one of their putative optical counterparts, no matter which one, none of them can be considered a likely INS. Of course, at this stage we can not exclude a priori the possibility that some of the candidate optical counterparts are just unrelated field objects. In this case, the X-ray sources would turn out to be unidentified and their corresponding f_X/f_{opt} would increase, moving nearer to INS values. Overlooked INS candidates will be pinpointed after the systematic X-ray optical identification work, now in progress (La Palombara et al., in preparation).

7. Sources with no candidate optical counterpart

As a first step we decided to perform a selection within our sample by considering only the 125 X-ray sources with no candidate optical counterpart. To pinpoint more robust INS candidates we have to select those sources which have the highest value of the X-ray-to-optical flux ratio and, possibly, are characterized by a soft X-ray spectrum, and thus might be associated to Geminga-like neutron stars. According to

Table 6, all the typical classes of X-ray sources are characterized by $\log(f_X/f_{\text{opt}}) \lesssim 2$, since only the brightest extragalactic sources can exceed this flux ratio level (due to the problems described in §6, we ignore the case of the WDs). Therefore, we have decided to use $\log(f_X/f_{\text{opt}}) = 2$ as a threshold value and to select the sources whose flux ratio, taking into account also the relevant uncertainties, approaches to this value. In this way we can reject all the galactic sources, almost all the galaxies and clusters of galaxies and most of the AGNs. This selection limits our sample to 9 sources. For illustration purposes, Fig. 10 shows the positions of these sources overlaid on the *WFI* V -band images. The main characteristics of these sources are summarized in Table 7 where, for each source, we list the detection energy bands, its flux and the corresponding X-ray-to-optical ratio lower limit. We also report the more likely spectral parameters derived by comparing the source *HRs* with different template spectral models, namely: a thermal *bremsstrahlung*, with temperatures $kT_{br} = 0.5, 1, 2$ and 5 keV; a *blackbody*, with temperatures $kT_{bb} = 0.05, 0.1, 0.2$ and 0.5 keV; a *power-law*, with photon index $\Gamma = 1 - 2.5$.

As it is seen from Table 7, we have singled out 8 INS candidate counterparts associated to 3EG J0616–3310. While all of them are potential candidates, XMMU J061807.6-331237 is certainly more interesting as it meets both our selection criteria, since it is characterized both by a relatively high X-ray-to-optical flux ratio ($> 1.73 \pm 0.31$) and by a soft emission spectrum (it is detected only below 1 keV). Therefore this source appears a promising candidates for a Geminga-like INS. On the other hand, XMMU J061429.8-333225 and XMMU J061450.2-331501, which are both detected in *EPIC* field # 3, stand out as the only sources with an X-ray-to-optical flux ratio clearly greater than 2 ($> 2.48 \pm 0.24$ and

Table 7. Main characteristics of the X-ray sources with no candidate optical counterpart and $\log(f_X/f_{\text{opt}}) \gtrsim 2$.

(1) OBS	(2) SRC	(3) DETECTION BANDS (keV)	(4) kT _{br} (keV)	(5) kT _{bb} (keV)	(6) Γ	(7) Flux (10 ⁻¹⁴ cgs)	(8) f_X/f_{opt} (log)
2	XMMU J061807.6-331237	0.5-1	≤ 5	0.2	≥ 1	2.28 ± 1.23	1.73 ± 0.31
3	XMMU J061429.8-333225	0.5-2; 0.5-1; 1-2	≥ 2	0.5	1-2.5	12.92 ± 3.67	2.48 ± 0.24
3	XMMU J061450.2-331501	0.5-2; 1-2	2-5	> 0.2	1.5-2	5.14 ± 2.21	2.08 ± 0.27
3	XMMU J061526.1-331724	0.5-2; 1-2	≥ 2	> 0.2	1-2	3.22 ± 1.12	1.88 ± 0.25
3	XMMU J061546.9-333347	1-2	≥ 1	≥ 0.2	≤ 2.5	1.93 ± 1.03	1.66 ± 0.31
4	XMMU J061507.9-330026	0.5-2; 2-10; 1-2; 2-4.5	> 5	> 0.5	≤ 1	3.67 ± 1.18	1.93 ± 0.24
4	XMMU J061557.2-324635	0.5-2; 1-2	0.5-5	0.2-0.5	2-2.5	2.95 ± 1.47	1.84 ± 0.29
4	XMMU J061504.5-330533	0.5-2	≤ 5	> 0.2	≥ 1.5	2.06 ± 1.41	1.68 ± 0.36
8	XMMU J124642.5-832212	2-10	> 5	> 0.5	< 1	3.62 ± 1.69	1.77 ± 0.20

Key to Table - Col.(1): *EPIC* field sequential reference number. Col. (2): Source identification. Col. (3): Source Detection Bands, i.e. the energy ranges j where the probability $P(j)$ that the source counts are due to a background fluctuation is lower than 2×10^{-4} (see text). Col. (4): Estimated range of possible kT_{br} temperatures for a thermal bremsstrahlung spectrum (i.e. XSPEC *wabs bremss* model) compatible with the measured *HRs*. Col. (5): Estimated range of possible kT_{bb} temperatures for a thermal blackbody spectrum (i.e. XSPEC *wabs bbody* model) compatible with the measured *HRs*. Col. (6): Estimated range of photon index Γ values for a power law spectrum (i.e. XSPEC *wabs pow* model) compatible with the measured *HRs*. In all cases, we assumed the galactic N_{H} estimated in the pointing direction (Table 1). The wide range of values for the spectral parameters kT_{br}, kT_{bb} and Γ are due to the low count statistics and to the large error bars on the derived source *HRs*. Col. (7): Estimated source flux in the energy range 0.3–10 keV, assuming a power law spectrum with $\Gamma = 1.7$ and the galactic N_{H} in the pointing direction. Col. (8): Lower limit (in logarithmic units) of the X-ray-to-optical ratio, assuming the X-ray flux of column (6) and the derived optical flux upper limits.

$> 2.08 \pm 0.27$, respectively). However, both sources are detected up to 2 keV while they are not seen below 0.5 keV. As a result, their hardness ratios correspond to a *thermal blackbody* temperature greater than 0.2 keV or to a *power-law* photon index $\Gamma = 1 - 2.5$. These values would point towards younger objects than Geminga-like INSSs. Indeed, Becker & Trümper (1997) have shown that the power-law components of X-ray detected INSSs have average photon index of ~ 1.9 , compatible with those estimated for sources XMMU J061429.8-333225 and XMMU J061450.2-331501. Thus, we consider XMMU J061807.6-331237, XMMU J061429.8-333225 and XMMU J061450.2-331501 our best INSS candidate counterparts to 3EG J0616–3310. Owing to the shallower optical coverage of the 3EG J1249–8330 error box (see table 4), we could single out only one possible INSS candidate counterpart (XMMU J124642.5-832212). The X-ray spectral parameters of this source are unconstrained but they suggest a rather hard thermal spectrum which would not be compatible either with a Geminga-like or with a young INSSs. However, the X-ray-to-optical flux ratio of this source ($> 1.77 \pm 0.02$), similar to the one of XMMU J061807.6-331237, still makes it a possible INSS candidate.

8. Summary and conclusions

Identifying high-energy γ -ray sources is a difficult and time-consuming task, owing primarily to the dimension of the error boxes that have to be covered at different wavelengths. We have developed a semiautomatic procedure, encompassing *ad-hoc* X-ray space observations as well as optical ground based ones, aimed at finding high f_X/f_{opt} candidate counterparts and we have applied it to two middle latitude *EGRET* sources. We have mapped the error boxes of 3EG J0616–3310 and 3EG J1249–8330 with eight 10 ksec *XMM-Newton* pointings and

we have detected about 300 X-ray sources between 0.3 and 10 keV, down to flux limits of $\sim 4 \times 10^{-15}$ and $\sim 2 \times 10^{-14}$ erg cm⁻² s⁻¹ in the energy ranges 0.5–2 and 2–10 keV, respectively. Four of the eight *XMM-Newton* pointings have been covered in the optical with the *Wide Field Imager (WFI)* at the 2.2m MPG/ESO telescope (La Silla) down to a limiting magnitude of $V \sim 24.5$. For the remaining fields, optical coverage down to $B_J \sim 23$ has been provided by the *GSC-2.3*. For all fields, the *2MASS* catalogue was also used to extend the available colour coverage in the near IR in order not to miss possible very reddened counterparts. For about 50 % of the detected X-ray sources we found candidate counterparts which yield X-ray-to-optical flux ratios comparable with the typical range of values of the known X-ray source classes. From the sample of the X-ray sources with no identification we have selected 9 sources (8 associated to the 3EG J0616–3310 error box and 1 to the 3EG J1249–8330 one) characterized by X-ray-to-optical flux ratios greater than 100. Although all the selected X-ray sources can be considered viable candidate counterparts to the two *EGRET* sources, we are not yet in the position to propose robust INSS identifications. However, we have singled out three interesting sources (XMMU J061807.6-331237, XMMU J061429.8-333225 and XMMU J061450.2-331501) which are particularly promising counterparts to 3EG J0616–3310 and certainly worth further optical investigations.

While we shall pursue the study of our candidate counterparts, we note that the need to characterize hundreds of X-ray and optical sources, just to discard them, is an unavoidable bottleneck, limiting the efficiency of any multiwavelength approach. Since the number of serendipitous, unrelated sources is proportional to the surface covered, a significant step forward will be possible only reducing the dimension of the γ -ray error boxes. The next generation high energy gamma ray telescopes,

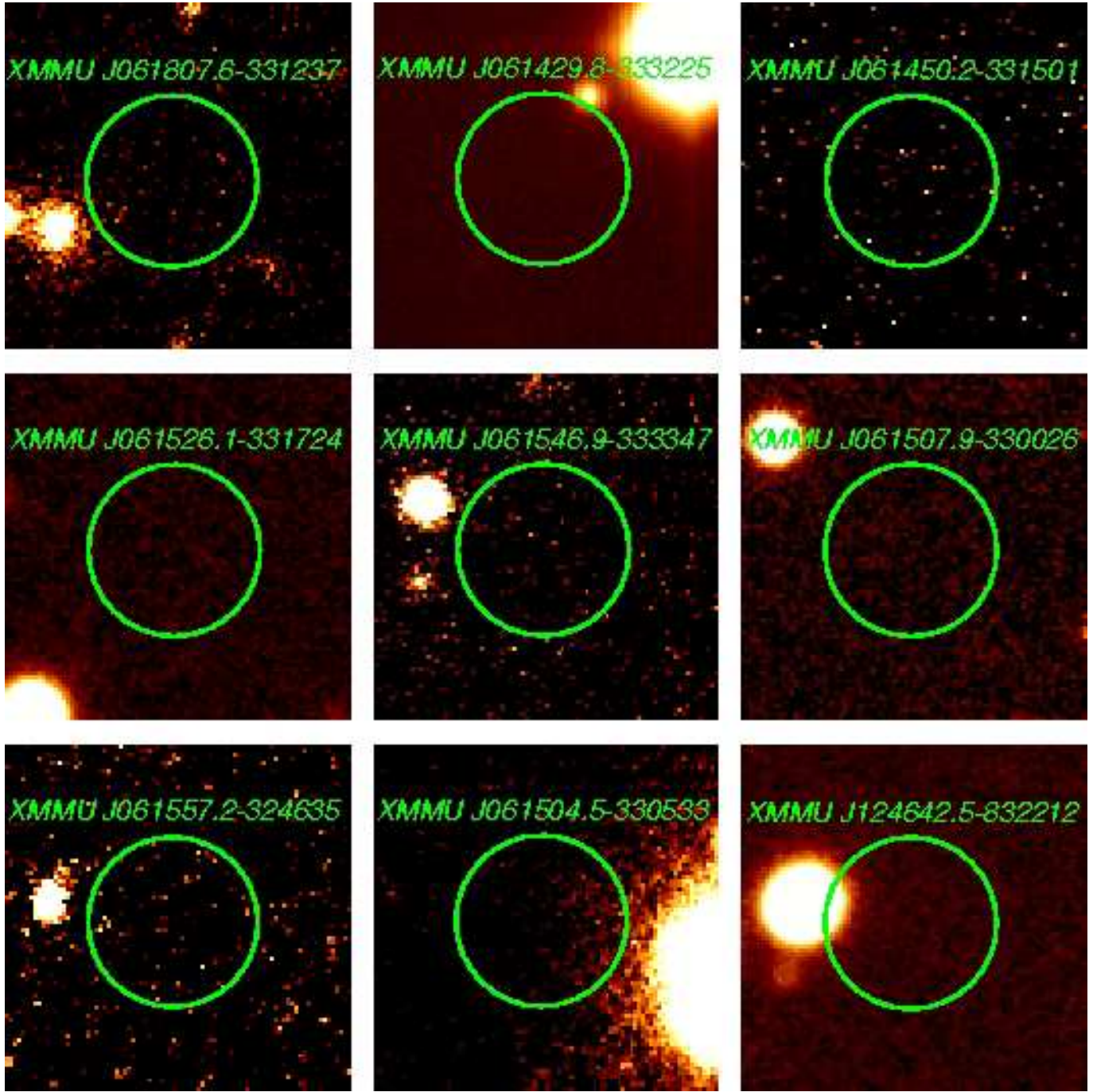


Fig. 10. Finding charts of the X-ray sources listed in Table 7. For each source the 5'' radius error circle is superimposed on the corresponding V-band WFI image.

AGILE and *GLAST*, promise to improve the source positioning, thus significantly reducing the uncertainty region associated to each source. Smaller error boxes can be covered with less X-ray and optical pointings, thus reducing both the observing time and the number of sources in need of a thorough characterization. Hopefully, this will mark a turning point in the long struggle towards the identification of the UGOs both as individual sources and as a population.

Acknowledgements. We wish to thank M. Chieregato, A. De Luca and S. Mereghetti for their useful comments and suggestions. We also thank S. Ghizzardi, M. Uslenghi and S. Vercellone for their tech-

nical support. The *XMM-Newton* data analysis is supported by the Italian Space Agency (ASI), through contract ASI/INAF I/023/05/0. The Guide Star Catalog used in this work was produced at the Space Telescope Science Institute under U.S. Government grant. These data are based on photographic data obtained using the Oschin Schmidt Telescope on Palomar Mountain and the UK Schmidt Telescope. This publication makes use of data products from the Two Micron All Sky Survey, which is a joint project of the University of Massachusetts and the Infrared Processing and Analysis Center/California Institute of Technology, funded by the National Aeronautics and Space Administration and the National Science Foundation.

References

Aharonian, F., Akhperjanian, A. G., Aye, K.-M., et al. 2005a, *Science*, 307, 1938

Aharonian, F., Akhperjanian, A. G., Aye, K.-M., et al. 2005b, *A&A*, 435, L17

Aharonian, F., Akhperjanian, A. G., Aye, K.-M., et al. 2005c, *A&A*, 439, 1013

Aharonian, F., Akhperjanian, A. G., Bazer-Bachi, A. R., et al. 2005d, *A&A*, 437, L7

Baldi, A., Molendi, S., Comastri, A., et al. 2002, *ApJ*, 564, 190

Barcons, X., Carrera, F. J., Watson, M. G., et al. 2002, *A&A*, 382, 522

Becker, W. & Trümper, J. 1997, *A&A*, 326, 682

Bergeron, P., Wesemael, F., & Beauchamp, A. 1995, *PASP*, 107, 1047

Bertin, E. & Arnouts, S. 1996, *A&AS*, 117, 393

Bhattacharya, D., Akyüz, A., Miyagi, T., Samimi, J., & Zych, A. 2003, *A&A*, 404, 163

Bignami, G. F. & Caraveo, P. A. 1996, *ARA&A*, 34, 331

Brazier, K. T. S., Kanbach, G., Carraminana, A., Guichard, J., & Merck, M. 1996, *MNRAS*, 281, 1033

Brazier, K. T. S., Reimer, O., Kanbach, G., & Carraminana, A. 1998, *MNRAS*, 295, 819

Brogan, C. L., Gaensler, B. M., Gelfand, J. D., et al. 2005, *ApJ*, 629, L105

Camilo, F., Bell, J. F., Manchester, R. N., et al. 2001, *ApJ*, 557, L51

Caraveo, P. A. 2001, *AIP Conf. Proc.* 587: ‘Gamma-Ray Astrophysics 2001’, 641

Caraveo, P. A. 2002, Proceedings of the XXII Moriond Astrophysics Meeting ‘The Gamma-Ray Universe’ (Les Arcs, March 9-16, 2002), eds. A. Goldwurm, D. Neumann, and J. Tran Thanh Van, The Gioi Publishers, 371

Caraveo, P. A., Bignami, G. F., & Trümper, J. E. 1996, *A&A Rev.*, 7, 209

Casandjian, J. M., Grenier, I. A., & Terrier, R. 2005, SF2A-2005: ‘Semaine de l’Astrophysique Francaise’, ed. F. Casoli, T. Contini, J. M. Hameury, & L. Pagani, 573

Casares, J., Ribas, I., Paredes, J. M., Martí, J., & Allende Prieto, C. 2005, *MNRAS*, 360, 1105

Chieregato, M. 2005, Ph.D. Thesis

Combi, J. A., Ribó, M., Mirabel, I. F., & Sugizaki, M. 2004, *A&A*, 422, 1031

Combi, J. A., Romero, G. E., Paredes, J. M., Torres, D. F., & Ribó, M. 2003, *ApJ*, 588, 731

Condon, J. J., Cotton, W. D., Greisen, E. W., et al. 1998, *AJ*, 115, 1693

Cutri, R. M., Skrutskie, M. F., van Dyk, S., et al. 2003, *VizieR Online Data Catalog*, 2246

D’Amico, N., Kaspi, V. M., Manchester, R. N., et al. 2001, *ApJ*, 552, L45

Erben, T., Schirmer, M., Dietrich, J. P., et al. 2005, *Astronomische Nachrichten*, 326, 432

Esa. 1997, *VizieR Online Data Catalog*, 1239

Gehrels, N., Macomb, D. J., Bertsch, D. L., Thompson, D. J., & Hartman, R. C. 2000, *Nature*, 404, 363

Giacconi, R., Rosati, P., Tozzi, P., et al. 2001, *ApJ*, 551, 624

Grenier, I. A. 2000, *A&A*, 364, L93

Grenier, I. A. 2001, *ASSL Vol. 267: ‘The Nature of Unidentified Galactic High-Energy Gamma-Ray Sources’*, 51–63

Grenier, I. A. 2004, in ‘Cosmic Gamma-ray Sources’, edited by K.S. Cheng and G.E. Romero, Kluwer Academic Press, 2004

Halpern, J. P., Camilo, F., Gotthelf, E. V., et al. 2001a, *ApJ*, 552, L125

Halpern, J. P., Eracleous, M., Mukherjee, R., & Gotthelf, E. V. 2001b, *ApJ*, 551, 1016

Halpern, J. P., Gotthelf, E. V., Camilo, F., Helfand, D. J., & Ransom, S. M. 2004, *ApJ*, 612, 398

Halpern, J. P., Gotthelf, E. V., Leighly, K. M., & Helfand, D. J. 2001c, *ApJ*, 547, 323

Halpern, J. P., Gotthelf, E. V., Mirabal, N., & Camilo, F. 2002, *ApJ*, 573, L41

Hartman, R. C., Bertsch, D. L., Bloom, S. D., et al. 1999, *ApJS*, 123, 79

Hayes, D. S. 1985, *IAU Symp.* 111: ‘Calibration of Fundamental Stellar Quantities’, 225–249

Henden, A. A. & Honeycutt, R. K. 1995, *PASP*, 107, 324

Jansen, F., Lumb, D., Altieri, B., et al. 2001, *A&A*, 365, L1

Kaaret, P., Cusumano, G., & Sacco, B. 2000, *ApJ*, 542, L41

Kanbach, G., Bertsch, D. L., Dingus, B. L., et al. 1996, *A&AS*, 120, C461

Kaspi, V. M., Lackey, J. R., Mattox, J., et al. 2000, *ApJ*, 528, 445

Kirsch, M. G. F., Altieri, B., Chen, B., et al. 2004, *SPIE Proceedings* 5488, 103–114

Krautter, J., Zickgraf, F.-J., Appenzeller, I., et al. 1999, *A&A*, 350, 743

Kuiper, L., Hermsen, W., Verbunt, F., et al. 2002, *ApJ*, 577, 917

La Palombara, N., Caraveo, P., Mignani, R., et al. 2005, *Ap&SS*, 297, 335

Manchester, R. N., Lyne, A. G., Camilo, F., et al. 2001, *MNRAS*, 328, 17

Massi, M. 2004, *A&A*, 422, 267

Mattox, J. R., Hartman, R. C., & Reimer, O. 2001, *ApJS*, 135, 155

McEnery, J. E., Moskalenko, I. V., & Ormes, J. F. 2004, *ASSL Vol. 304: ‘Cosmic Gamma-Ray Sources’*, 361

McSwain, M. V., Gies, D. R., Huang, W., et al. 2004, *ApJ*, 600, 927

Mirabal, N. & Halpern, J. P. 2001, *ApJ*, 547, L137

Moro, D. & Munari, U. 2000, *A&AS*, 147, 361

Mukherjee, R., Halpern, J., Mirabal, N., & Gotthelf, E. V. 2002, *ApJ*, 574, 693

Mukherjee, U. & Halpern, J. P. 2004, in ‘Cosmic Gamma-ray Sources’, edited by K.S. Cheng and G.E. Romero, Kluwer Academic Press, 2004,

Nolan, P. L., Tompkins, W. F., Grenier, I. A., & Michelson, P. F. 2003, *ApJ*, 597, 615

Prugniel, P. & Heraudeau, P. 1998, *VizieR Online Data Catalog*, 7206

Reid, I. N., Brewer, C., Brucato, R. J., et al. 1991, *PASP*, 103, 661

Reimer, O., Brazier, K. T. S., Carramiñana, A., et al. 2001,

MNRAS, 324, 772

Roberts, M. S. E. 2005, Advances in Space Research, 35, 1142

Roberts, M. S. E., Brogan, C. L., Gaensler, B. M., et al. 2005, Ap&SS, 297, 93

Roberts, M. S. E., Gaensler, B. M., & Romani, R. W. 2002a, ASP Conf. Ser. 271: 'Neutron Stars in Supernova Remnants', 213

Roberts, M. S. E., Hessels, J. W. T., Ransom, S. M., et al. 2002b, ApJ, 577, L19

Roberts, M. S. E., Romani, R. W., & Kawai, N. 2001, ApJS, 133, 451

Romero, G. E. 2001, ASSL Vol. 267: 'The Nature of Unidentified Galactic High-Energy Gamma-Ray Sources', 65–80

Romero, G. E., Benaglia, P., & Torres, D. F. 1999, A&A, 348, 868

Romero, G. E. & et al. 2004, ESA SP-552: '5th INTEGRAL Workshop on the INTEGRAL Universe', ed. V. Schoenfelder, G. Lichten, & C. Winkler, 703

Romero, G. E., Kaufman Bernadó, M. M., Combi, J. A., & Torres, D. F. 2001, A&A, 376, 599

Schirmer, M., Erben, T., Schneider, P., et al. 2003, A&A, 407, 869

Schlegel, D. J., Finkbeiner, D. P., & Davis, M. 1998, ApJ, 500, 525

Severgnini, P., Della Ceca, R., Braito, V., et al. 2005, A&A, 431, 87

Sguera, V., Bassani, L., Malizia, A., et al. 2005, A&A, 430, 107

Sguera, V., Malizia, A., Bassani, L., Stephen, J. B., & Di Cocco, G. 2004, A&A, 414, 839

Sowards-Emmerd, D., Romani, R. W., Michelson, P. F., & Ulvestad, J. S. 2004, ApJ, 609, 564

Stocke, J. T., Morris, S. L., Gioia, I. M., et al. 1991, ApJS, 76, 813

Strüder, L., Briel, U., Dennerl, K., et al. 2001, A&A, 365, L18

Tavani, M., Barbiellini, G., Argan, A., et al. 2003, SPIE Proceedings 4851: 'X-Ray and Gamma-Ray Telescopes and Instruments for Astronomy', 2003, pp. 1151-1162

Thompson, D. J. 2004, in 'Cosmic Gamma-ray Sources', edited by K.S. Cheng and G.E. Romero, Kluwer Academic Press, 2004

Tornikoski, M., Lähteenmäki, A., Lainela, M., & Valtaoja, E. 2002, ApJ, 579, 136

Torres, D. F. & Reimer, O. 2005, ApJ, 629, L141

Torres, D. F., Romero, G. E., Combi, J. A., et al. 2001a, A&A, 370, 468

Torres, D. R., Pessah, M. E., & Romero, G. E. 2001b, Astronomische Nachrichten, 322, 223

Turner, M. J. L., Reeves, J. N., Ponman, T. J., et al. 2001, A&A, 365, L110

Veron-Cetty, M. P. & Veron, P. 2003, VizieR Online Data Catalog, 7235

von Montigny, C., Bertsch, D. L., Chiang, J., et al. 1995, ApJ, 440, 525

Wallace, P. M., Halpern, J. P., Magalhães, A. M., & Thompson, D. J. 2002, ApJ, 569, 36

Wright, A. & Otrupcek, R. 1990, PKS Catalog, 1990, 0

Wright, A. E., Griffith, M. R., Burke, B. F., & Ekers, R. D. 1994, ApJS, 91, 111

Wright, A. E., Griffith, M. R., Hunt, A. J., et al. 1996, ApJS, 103, 145

Yadigaroglu, I.-A. & Romani, R. W. 1997, ApJ, 476, 347

Zickgraf, F.-J., Engels, D., Hagen, H.-J., Reimers, D., & Voges, W. 2003, A&A, 406, 535

Zickgraf, F.-J., Thiering, I., Krautter, J., et al. 1997, A&AS, 123, 103

Zombeck, M. V. 1990, 'Handbook of space astronomy and astrophysics' (Cambridge University Press, 1990, 2nd ed.)

Table A.1. Range of the applicable $B - V$ colours for the selected classes of objects

CLASS	(B-V) min	(B-V) max	REFERENCE
Stars	-0.2	+1.8	Esa (1997)
WDs	-0.3	+1.6	Bergeron et al. (1995)
CVs	+0.2	+2.0	Henden & Honeycutt (1995)
Galaxies	+0.2	+1.6	Prugniel & Heraudeau (1998)
Clusters	+1.0	+1.5	Chieregato (2005)
AGN	-0.6	+1.6	Veron-Cetty & Veron (2003)

Appendix A: Correction of the Classification Scheme

According to Chieregato (2005), for each class of sources the f_X/f_{opt} in the *XMM-Newton* is obtained from the corresponding *Hamburg/RASS* one as follows:

$$\frac{f_{X,\text{XMM}}}{f_B} = \frac{f_{X,\text{Hamburg-RASS}}}{f_B} \times \frac{f_{X,\text{XMM}}}{f_{X,\text{Hamburg-RASS}}} \quad (\text{A.1})$$

We considered separately the corrections due to the different energy ranges and to the different spectral models:

$$\begin{aligned} \frac{f_{X,\text{XMM}}}{f_{X,\text{Hamburg-RASS}}} &= \frac{f_{0.3-10,\text{PL}}}{f_{0.1-2.4,\text{MOD}}} = \\ \frac{f_{0.3-10,\text{PL}}}{f_{0.1-2.4,\text{PL}}} \times \frac{cf_{0.1-2.4,\text{PL}}}{cf_{0.1-2.4,\text{MOD}}} \end{aligned} \quad (\text{A.2})$$

For each of the eight *XMM-Newton* pointings we estimated both the flux ratio $f_{0.3-10,\text{PL}}/f_{0.1-2.4,\text{PL}}$ and the conversion factor $cf_{0.1-2.4,\text{PL}}$. In addition, for each class of sources we estimated also the specific conversion factor $cf_{0.1-2.4,\text{MOD}}$.

The $f_{X,\text{XMM}}/f_V$ values were obtained from the $f_{X,\text{XMM}}/f_B$ ones according to the relation:

$$\frac{f_{X,\text{XMM}}}{f_V} = \frac{f_{X,\text{XMM}}}{f_B} \times \frac{f_B}{f_V} \quad (\text{A.3})$$

where

$$\frac{f_B}{f_V} = \frac{f_{B,\text{Vega}}}{f_{V,\text{Vega}}} \times 10^{-(B-V)/2.5} = 1.957 \times 10^{-(B-V)/2.5} \quad (\text{A.4})$$

For each class of celestial source we considered the range of $B - V$ colours which include 99 % of the total sample (see Table A.1).

For candidate counterparts with only *GSC-2.3* photometry, we considered the correction factor for the different blue magnitude:

$$\frac{f_{X,\text{XMM}}}{f_{B_J}} = \frac{f_{X,\text{XMM}}}{f_B} \times \frac{f_B}{f_{B_J}} \quad (\text{A.5})$$

where:

$$\frac{f_B}{f_{B_J}} = \frac{f_{B,\text{Vega}}}{f_{B_J,\text{Vega}}} \times 10^{-\frac{B-B_J}{2.5}} = 0.822 \times 10^{-\frac{B-B_J}{2.5}} \quad (\text{A.6})$$

and $B - B_J = 0.28 \times (B - V)$ (Reid et al. 1991). Also in this case we referred to Table A.1 for the $B - V$ colours of each class of source.

Appendix B: Measurement of the X-ray-to-optical flux ratios

We computed the $f_{X,\text{XMM}}/f_{opt}$ ratios for all the candidate counterparts. X-ray fluxes are the same determined in §3.4 while optical fluxes were obtained from the measured *WFI* magnitudes using the Pogson formula $f_m = f_{m=0} \times 10^{-m/2.5}$, assuming $f_{m=0} = 2.904, 6.478, 3.240, 3.828$ and 1.997×10^6 erg cm $^{-2}$ s $^{-1}$ for $m = U, B, V, R$ and I passbands, respectively (Zombeck 1990).

Since for the B_J band, there is no simple relation to obtain the optical flux, we first estimated its Vega band flux. This is given by the relation $f_{B_J=0} = f_{\lambda_{\text{eff}}(B_J)} \times W_{\text{eff}}(B_J)$, where $\lambda_{\text{eff}}(B_J)$ and $W_{\text{eff}}(B_J)$ are, respectively, the effective wavelength and width of the filter, while $f_{\lambda_{\text{eff}}(B_J)}$ is the specific flux calibration at $\lambda_{\text{eff}}(B_J)$ for $B_J = 0$. By referring to the *Asiago Database on Photometric Systems* (Moro & Munari 2000) we found $\lambda_{\text{eff}}(B_J) = 4731$ Å and $W_{\text{eff}}(B_J) = 1333$ Å. In order to obtain the specific flux calibration f_{4731} , we considered the spectral distribution of Vega provided by Hayes (1985) and performed a linear interpolation between 4725 and 4750 Å. In such a way we obtained $f_{4731} = 5.457 \times 10^{-9}$ erg cm $^{-2}$ s $^{-1}$ Å $^{-1}$ and $f_{B_J=0} = 1333 \times 5.457 \times 10^{-9} = 7.274 \times 10^{-6}$ erg cm $^{-2}$ s $^{-1}$. Finally, we used the Pogson formula $f_{B_J} = f_{B_J=0} \times 10^{-B_J/2.5}$ to obtain the optical flux for a given magnitude B_J . In the case of the F band magnitude, we applied the same procedure but assuming $\lambda_{\text{eff}}(F) = 6555$ Å, $W_{\text{eff}}(F) = 767$ Å and $f_{6555} = 1.731 \times 10^{-9}$ erg cm $^{-2}$ s $^{-1}$ Å thus obtaining $f_F = 1.328 \times 10^{-6} \times 10^{-F/2.5}$ erg cm $^{-2}$ s $^{-1}$.